GEOPHYSICS®

Stress path dependent velocities in shales: Impact on 4D seismic interpretation

Journal:	*Geophysics*
Manuscript ID	GEO-2017-0652
Manuscript Type:	Discussion
Date Submitted by the Author:	03-Oct-2017
Complete List of Authors:	Holt, Rune; NTNU, Dept. of Geoscience & Petroleum Bauer, Andreas; SINTEF Petroleum Research Bakk, Audun; SINTEF Petroleum Research
Keywords:	rock physics, 4D, pore pressure, ultrasonic
Area of Expertise:	Rock Physics, Reservoir Geophysics

Stress Path Dependent Velocities in Shales:

Impact on 4D Seismic Interpretation

Running Title: Stress path dependence and 4D

Rune M. Holt[1], Andreas Bauer[1,2], Audun Bakk[2]

[1]NTNU (Norwegian University of Science and Technology), Trondheim, Norway

[2]SINTEF Petroleum Research, Trondheim, Norway

Email: rune.holt@ntnu.no

ABSTRACT

Overburden stresses and pore pressure are altered by depletion or inflation of a subsurface reservoir, leading to seismic travel time and reflectivity changes that may be interpreted as fingerprints of reservoir drainage or injection. The objective of this research is to contribute to quantification of expected 4D seismic timeshifts and reflectivities by understanding how overburden stresses change and how seismic velocities depend on these stress changes. Ultrasonic stress sensitivities of velocities have been obtained from controlled laboratory experiments where field shale cores are brought to in situ conditions and then probed along different stress paths. Comparing with the outcome of numerical geomechanical simulations of possible overburden stress paths resulting from elastic contrast between overburden and reservoir, or reservoir tilt, the response of in situ velocity to reservoir pore pressure change can be estimated along with strain sensitivity (dilation or *R*-factor). Both stress and strain sensitivities show significant stress path dependence. The *R*-factor is particularly sensitive to stress path, reflecting its explicit sensitivity to vertical in situ strain. The results also show that 4D overburden response may be significantly influenced by pore pressure changes in the overburden.

KEYWORDS

Rock physics, 4D, Pore pressure, Ultrasonic

INTRODUCTION

Elastic wave velocities in most rocks depend on stress. In porous rocks, changes in stress as well as changes in pore pressure cause velocities to change. For instance, when pore pressure is decreased by depletion, seismic velocities in the reservoir generally increase, and vice versa. This may be seen as a result of a change in effective stress as a result of the imposed change in reservoir pore pressure upon production. In order to predict time-lapse (4D) seismic response from core data, or to use 4D data to interpret subsurface changes, one needs to understand how seismic velocities depend on in situ pore pressure and associated stress changes within and around the reservoir.

Overburden stress changes due to pore pressure depletion have significant impact on 4D seismic time shifts and amplitudes (Kenter et al., 2004; Hatchell & Bourne, 2005; Røste et al, 2006; De Gennaro et al., 2008; Røste and Ke, 2017). This is in particular the case for the reflection from the top of a depleting reservoir, which is slowed down by vertical stress reduction due to stress arching in the overburden above the central part of the depleting area. This time shift is a footprint of reservoir depletion (or injection if this applies).

When stress sensitivity is measured in the laboratory, i.e. the relative change in velocity vs. change in stress, external stress and pore pressure can be controlled. The majority of such studies are performed with isotropic external stress and stress changes, and usually in drained (constant pore pressure) conditions. With shales, which are the main focus of this work, both drained (externally controlled pore pressure) and undrained (no pore fluid flow) tests segments may be applied. The drained tests are particularly time-consuming due to the low shale permeability. However, the relatively faster undrained tests, with monitoring of the pore pressure response are preferable for the overburden monitoring in the perspective of a field lifetime. The reason for this is that the response of the bulk overburden will in practice be undrained upon reservoir pressure changes due to its very low permeability (unless activation of higher permeable pathways as faults applies). The choice of well-defined stress changes (hereinafter termed: stress path) such as isotropic is convenient for purposes of comparing results between different rocks and different laboratories. On the other hand, a consequence is that the impact of different stress paths is often neglected and therefore is less understood. In particular, if laboratory experiments are done to solve a field related problem, the stress sensitivity along the specific in situ stress path is required.

The main objectives of this work are to demonstrate stress path dependence of ultrasonic velocities in controlled laboratory experiments, and to show how laboratory observations may be translated into 4D response. We first present an overview of previous experimental observations of stress dependence in shale, mostly with an isotropic stress path only. A few laboratory studies where different stress paths have been probed will be highlighted, including measurements with sandstone. Then we proceed to show how stress path dependence may be addressed through use of simple ad hoc models, and also how it can be derived within the frames of effective medium theories. Laboratory experiments will be presented where shale cores are brought to in situ stress and pore pressure conditions, and then loaded and unloaded along four different stress paths. The resulting stress path dependence of wave velocities and the related strain sensitivity (dilation) parameter R (defined below) will be analysed. In situ stress paths will be briefly discussed and described, with primary focus on the overburden above producing reservoirs or storage sites, and how they depend on geometry and elastic contrast between the depleted (or inflated) region and its surroundings. Implications for 4D seismic interpretation will be discussed, including the impact of pore pressure changes in the overburden.

EXPERIMENTAL BACKGROUND

Isotropic stress dependence of P-wave velocities in shale

Several studies of laboratory measured stress dependent wave velocities in shales have been published over the last few decades (Johnston, 1987; Jones and Wang, 1991; Johnston and Christensen, 1995; Hornby; 1998; Wang, 2002; Pervukhina et al., 2008). In all these studies, a drained isotropic stress path was applied, and ultrasonic frequencies were used. In one case, dry shales were studied (Johnston & Christensen, 1995), and pore pressure was not applied. Focussing on the P-wave velocity normal to bedding, the studies reveal the following characteristic features:

- Stress sensitivity is usually higher at low confining pressure (= radial stress) than at high stress levels, as can be seen in Figure 1. This observation points towards the role of pre-existing microcracks, which could have been introduced within the samples during coring.
- Stress sensitivity above 30 MPa net radial stress is close to constant (velocity change with stress is linear) (Figure 1). This is different from what is seen in e.g. sandstone, in the sense that the stress sensitivity in shale does not appear to converge to zero, even at stresses in the 100 MPa range. The most likely explanation is that shales deform under large stress by reducing porosity, whereas in sandstones, stress-insensitive cemented grain contacts carry the load.
- Stress sensitivity above 30 MPa net radial stress varies remarkably little from shale to shale, irrespective of whether they are dry or saturated. A typical value for the relative stress sensitivity is 10^{-3} MPa^{-1}.

- Johnston (1987) found lower stress sensitivity during unloading than during initial loading. This is what one would expect based on soil mechanics principles. In particular, the first loading of shale in a normal-consolidated state results in much larger stress sensitivity than unloading or reloading in an overconsolidated state. Most of this can be attributed to large irreversible porosity loss during normal consolidation.
- From Johnston (1987) it also seems that different temperatures (25 vs. 100 °C) may play only a minor role for stress sensitivity.

Laboratory stress paths

In the laboratory, it is convenient to introduce a stress path parameter (κ) that describes the relative change of radial stress and axial stress:

$$\kappa = \frac{\Delta\sigma_r}{\Delta\sigma_z}, \tag{1}$$

where σ denotes total stresses, with indexes r and z referring to the radial and axial directions of a cylindrical core, respectively. The isotropic (hydrostatic) stress path will have $\kappa = 1$. Amongst stress path paths commonly probed in a conventional triaxial set-up are uniaxial stress changes ($\kappa = 0$; often referred to as a triaxial stress path) and uniaxial strain (in soil mechanics termed K_0 (or oedometric), where the value of $\kappa = K_0$ is a property of the sample). Additionally, we also include the constant mean stress (CMS) path, where $\kappa = -$ ½.

Experimental evidence for stress path dependence

Very few studies of shales have been published where other stress paths than isotropic have been studied systematically. Dewhurst and Siggins (2006) showed experiments with brine-saturated Muderong Shale along a triaxial stress path. The results were however not compared with experiments with the same shale along other stress paths. Holt et al. (2008) and Holt and Fjær (2009) showed, in addition to differences between loading and unloading, stress path dependence of the strain sensitivity of the vertical P-wave velocity, expressed by the so-called

R-factor (Hatchell and Bourne, 2005; Røste et al., 2006). For P-waves travelling in the axial (z) direction with velocity v_{Pz}, the R-factor is:

$$R_{Pz} = \frac{\Delta v_{Pz}}{v_{Pz}\Delta\varepsilon_z} . \qquad (2)$$

Here $\Delta\varepsilon_z$ denotes axial strain (positive in compaction).

These tested materials included uncemented glass beads, artificial sandstone cemented under stress, brine-saturated kaolinite compacted under stress, and field shale. Figure 2 shows the timeline of stresses and pore pressure during an experiment with 3.5 weight % NaCl brine-saturated kaolinite (further description is given in Holt et al., 2013): The clay minerals were compacted to a fictitious in situ anisotropic stress state (23 MPa axial[1] and 20 MPa radial stress, with 10 MPa pore pressure). During this compaction, the axial stress was first increased stepwise to 10 MPa in drained uniaxial strain (K_0) conditions, keeping the pore pressure at 2 MPa, with measured radial stress response. Then the axial and radial stresses were both set to 10 MPa, and the pore pressure was increased to 4 MPa, followed by drained hydrostatic loading until the axial and radial stresses were both 14 MPa. The stresses and the pore pressure were then increased in equal steps (constant net stress conditions) to 20 and 10 MPa, respectively. After isotropic unloading and reloading, the axial stress was increased to 23 MPa. The undrained constant mean stress parts of the test were then performed from this "in situ" stress, first by lowering the axial and increasing the radial stress to mimic the effect of depletion, and then by increasing axial and decreasing radial stress to mimic the effect of injection into a storage reservoir beneath the compacted clay "cap rock". The choice of a constant mean stress path was based on the analytical model by Geertsma (1973) for a case

---

[1] The terms axial (z) and radial (r) refers to the experimental setup where cylindrical plugs are applied with stresses applied along the symmetry axis (axially = z-direction) and isotropically in the horizontal plane (radially = r-direction). In the field we refer to vertical and horizontal planes which is similar to the experimental axial and radial plane in case when the plugs are drilled normal to the bedding plane (for shales) as in present work.

where there is no elastic contrast between a reservoir and its surroundings. The data show (Figure 3), as was seen with glass beads and artificially cemented sandstone, that the *R*-factor is much larger during isotropic loading than along a K_0 stress path. The stress sensitivities recorded during the CMS segments are much smaller, but cannot be compared directly, since these were obtained under undrained conditions. Notice that axial loading and radial unloading leads to $R \approx 0$, which is a sign of non-elastic (yielding) behaviour of the compacted clay.

Actually, few experiments showing stress path sensitivity of wave velocities are published, even when other types of rocks are considered. A similar result was found by Scott (2007) for Berea sandstone. One of the most complete data sets was given by Dillen et al. (1999), based on experiments by Cruts et al. (1995), who applied multiple stress paths to a single core sample of Colton sandstone. Their data have been replotted to produce the trend shown in Figure 4. Note that the first two segments, representing initial loading, are not included, since stress sensitivity is much larger during initial loading than in subsequent segments. The increase in stress sensitivity with stress path is consistent with the behaviour of the compacted clay seen in Figure 3.

THEORETICAL CONCEPTS

Linear stress sensitivity

As seen above, shales often exhibit velocities that change proportionally with stress, at least at stress levels that are well above ambient conditions. With small stress changes near the in situ stress state, as one may expect above a depleting or inflating reservoir, linearity probably gives an adequate description of the shale behaviour. However; the coefficients will in general differ between scenarios of vertical stress increase above previously applied stress (associated with reservoir inflation), vertical stress decrease (associated with reservoir depletion) or reloading after stress decrease. One may express velocity changes for each P- and S-mode (denoted by subscript Q; being P or S) in each direction (denoted by subscript j; being z or r) by the following linearized form:

$$\frac{\Delta v_{Qj}}{v_{Qj}} = A_{Qj}\Delta\bar{\sigma} + B_{Qj}\Delta(\sigma_1 - \sigma_3) - C_{Qj}\Delta p_f \tag{3}$$

The decomposition into mean stress ($\Delta\bar{\sigma}$), shear stress ($\Delta(\sigma_1 - \sigma_3)$ (where σ_1 is maximum and σ_3 is minimum principal stress) and pore pressure changes (Δp_f) is assumed to account for the main physical mechanisms responsible for stress sensitivity. With at least three different stress paths being probed, the coefficients A_{Qj}, B_{Qj} and C_{Qj} can be determined from the experiments. As mentioned above, these coefficients may also depend on the scenario being initial loading, unloading or reloading. If these coefficients are known, velocity changes along any stress path may be computed.

Dropping subscripts (for simplicity; similar relationships apply to all modes), the velocity dependence of axial stress change (denoted S_z) can be written, by introducing the relation in Eq. (1) into Eq. (3):

$$S_z = \frac{\Delta v}{v\Delta\sigma_z} = \frac{1+2\kappa}{3}A + (1-\kappa)B - C\frac{\Delta p_f}{\Delta\sigma_z}. \tag{4}$$

If the pore pressure change is not known; i.e. if it is not measured during the test, we may calculate it if Skempton's A_s and B_s parameters, defined by (Skempton, 1954), are known:

$$\Delta p_f = B_S\left[\Delta\sigma_3 + A_S(\Delta\sigma_1 - \Delta\sigma_3)\right]. \tag{5}$$

Assuming the stress state is triaxial; with vertical (axial) stress (in the z- direction) and isotropic horizontal stress in the radial (r) plane, the stress sensitivity of the pore pressure is:

$$\frac{\Delta p_f}{\Delta\sigma_z} = A_S B_S + B_S(1-A_S)\kappa, \tag{6}$$

where κ from Eq. (1) is inserted. Inserting Eq. (6) into Eq. (4) leads to:

$$S_z = \frac{\Delta v}{v\Delta\sigma_z} = [\frac{A}{3} + B - A_S B_S C] + [\frac{2A}{3} - B - B_S(1-A_S)C]\kappa. \tag{7}$$

In the laboratory, the pore pressure change in undrained tests is usually measured, so that Eq. (4) can be used directly.

Notice that according to Eq. (4), the velocity change can be written:

$$\frac{\Delta \mathrm{v}}{\mathrm{v}} \propto (\Delta\sigma_z - \frac{C}{\frac{1+2\kappa}{3}A + (1-\kappa)B}\Delta p_f) = \Delta\sigma_z - n\Delta p_f \ . \tag{8}$$

This shows that the effective stress coefficient n controlling velocities also is stress path dependent, since n is a function of κ. In the case of isotropic loading (κ = 1), the effective stress coefficient is simply:

$$n = \frac{C}{A} \ . \tag{9}$$

The approach above is based on nonlinear elasticity, similar to the one introduced by Prioul et al. (2004) for initially TI (Transversely Isotropic) media. In order to maintain simplicity, they reduced the number of nonlinear coefficients by assuming the third order elastic tensor controlling stress sensitivity to be implicitly isotropic. Thus, only three coefficients would be required in order to fit experimental data. It was further assumed that net stress controls velocities in the presence of pore pressure.

More physically based models that maintain the capability to predict stress path dependence are for example those of Sayers (2006) and Fjær (2007). Sayers describes elastic moduli through perturbations to the elements of the compliance tensor caused by deformation of microcracks and boundaries between grains. Key parameters are the normal and shear compliances of the inclusions. In Sayers (2006), the effect of stress path on P- and S-wave velocities were estimated for sandstone, where normal and shear compliances of microcracks are expected to be very similar. From the graphs found in Sayers' paper, the stress path dependences are like shown in Figure 5. Notice that Sayers assumes the microcrack or grain boundary compliances to be linear functions of net stress in rocks with pore pressure. Fjær (2007) included pores and three orthogonal crack distributions in an effective medium, where stress sensitivity originates in particular from stress dependent crack densities. The model incorporates crack closure as well as crack initiation, and was shown to be applicable for multiple stress paths. In Fjær (2007), anisotropic velocity changes during isotropic and triaxial loading beyond failure of a dry sandstone were computed, and found to agree with experimental data. This model was not applied to liquid-saturated rocks, and pore pressure effects were not included. Notice that in both these effective medium models, the material surrounding the inclusions is assumed to be isotropic. In both models Poisson's ratio (ν) of the surrounding material plays a vital role, in particular when ν becomes larger than 0.3. This is the case for several shales, where the surrounding material also exhibits anisotropy.

Strain sensitivity – the *R*-factor

The *R*-factor was introduced in Eq. (2). It describes the strain sensitivity of rock, and is convenient for 4D seismic because it can be determined on basis of measured change in two-way travel time (*TWT*) and subsidence / compaction data:

$$\frac{\Delta TWT}{TWT} = (1 + R_{\mathrm{Pz}})(-\Delta\varepsilon_{\mathrm{z}}) , \tag{10}$$

where R_{Pz} is given in Eq. (2).

Only vertical P-waves are considered in standard 4D seismic analysis, so we will focus on the strain sensitivity R_{Pz} only even though R may be formulated for any direction for both P- and S-waves. Clearly, this *R*-factor will also be stress path sensitive, as can be seen by reformulation of Eq. (2) and application of the stress sensitivity (S_{Pz}) as defined in Eq. (4):

$$R_{Pz} = \frac{\Delta \mathrm{v}_{Pz}}{\mathrm{v}_{Pz}\Delta\sigma_z}\left(\frac{\Delta\sigma_z}{\Delta\varepsilon_z}\right) = S_{Pz}\left(\frac{\Delta\sigma_z}{\Delta\varepsilon_z}\right) = S_{Pz}M_z , \tag{11}$$

where $M_z = \left(\frac{\Delta\sigma_z}{\Delta\varepsilon_z}\right)$ is the stress path dependent stiffness following directly from Hooke's law.

The stiffness can be given in terms of Young's moduli and Poisson's ratio for a TI medium (the expression in case of isotropic elasticity is also provided for completeness):

$$\frac{\Delta\sigma_z}{\Delta\varepsilon_z} = \frac{E_{\mathrm{V}}}{1-(\nu_{\mathrm{VH}}+\nu_{\mathrm{HV}})\frac{E_{\mathrm{V}}}{E_{\mathrm{H}}}\kappa} \text{(isotropic case: } = \frac{E}{1-2\nu\kappa}) \, . \tag{12}$$

Eqs. (11) and (12) show that *R* will increase with increasing stress path κ, even if there were no stress path dependence in the velocities themselves (Figure 6), simply because strain is extremely stress path sensitive. In the isotropic case, if Poisson's ratio approaches ½ (soft rock), the *R*-factor tends to diverge. The stiffness for each of the four stress paths applied in our work, in terms of TI stiffness matrix elements, are:

$$\left(\frac{\Delta\sigma_{\mathrm{z}}}{\Delta\varepsilon_{\mathrm{z}}}\right)_{\mathrm{iso}} = C_{33} + \frac{C_{13}(C_{33}-C_{13})}{C_{11}-C_{66}-C_{13}} \quad \text{(isotropic case: } =3K = \frac{E}{1-\nu}) , \tag{13}$$

$$\left(\frac{\Delta\sigma_z}{\Delta\varepsilon_z}\right)_{K_0} = C_{33} \quad (\text{isotropic case: } =H = E\frac{(1-\nu)}{(1+\nu)(1-2\nu)}), \qquad (14)$$

$$\left(\frac{\Delta\sigma_z}{\Delta\varepsilon_z}\right)_{3\text{ax}} = C_{33} - \frac{C_{13}^2}{C_{11}-C_{66}} \quad (\text{isotropic case: } =E), \qquad (15)$$

$$\left(\frac{\Delta\sigma_z}{\Delta\varepsilon_z}\right)_{\text{CMS}} = C_{33} - \frac{C_{13}(C_{33}+2C_{13})}{2(C_{11}-C_{66})+C_{13}} \quad (\text{isotropic case: } =2G = E\frac{1}{(1+\nu)}). \qquad (16)$$

Notice that the strain in Eq. (10) is static, so these are static stiffnesses. In general, static and dynamic stiffnesses are different (e.g. Holt et al., 2015). Thus, assuming elastic behavior and neglecting dispersion in geomechanical modeling tends to overestimate the stiffnesses and hence the *R*-factor.

EXPERIMENTS WITH FIELD SHALE CORES

Samples and laboratory method

Four different field shale cores have been tested. The cores were preserved (seal peeled) upon coring, and plugs were stored in Marcol (oil) prior to testing, in order to preserve natural humidity and saturation. Porosities vary from 9 to 36 % (from measured water loss after heating to 105 °C) and clay contents vary from 25 to 65 % (based on X–Ray diffraction (XRD) analysis). Three cores were pre-stressed, exposed to expected in situ brine salinity, and brought to stresses and pore pressure close to their respective in situ conditions (Table 1). This is expected to lead to full saturation (Horsrud et al., 1998). One shale ("T"-Shale) is a gas shale in situ, and was tested in as-received conditions, and with no applied pore pressure.

Laboratory tests were performed with 38 mm diameter and 50-60 mm long field shale core plugs in a triaxial set-up, with simultaneous pulse transmission measurements of multi-directional ultrasonic velocities (frequencies 500-600 kHz for P-waves; 125-250 kHz for S-waves). The uncertainty in the absolute value of the axial P-wave velocity is estimated to 1 %, being somewhat larger for the radial and oblique P-waves. S-wave velocities are difficult to measure accurately for soft high porosity shales, due to high absorption and thus strong interference with P-wave ringing. Measurements on shorter plugs are used as a guideline to picking correct S-wave arrivals, along with reduction in frequency. Relative changes in velocities as required for assessing stress sensitivity are however much more accurate. In the current experiments, axial P-wave velocity changes may be assessed within 0.1 %.

In all cases, the samples were prepared with their symmetry axis (z-axis) normal to the bedding plane. The tests were performed by loading the samples as close as possible to their in situ stress conditions (including in situ pore pressure) as stated in Table 1. During this loading, there is a sequence of drained loading followed by constant net stress loading, as was done for the kaolinite (Figure 2). In B, D and M Shales (see Figure 7 for an example of the mechanical timeline), these segments were performed after reaching the target stress state, followed by undrained loading-unloading cycles along 3 – 4 different stress paths (constant mean stress (CMS), isotropic (ISO), uniaxial strain (K_0), and triaxial (constant radial stress) (3AX)). With T shale, uniaxial strain cycles were not included. The axial stress changes were 5 MPa for B, D and M shales and 6 MPa for T shale. Changes in velocities and pore pressure plus axial and radial strains were monitored in all stages. The pore pressure was measured in a small (3 ml) dead volume, enabling accurate assessment of pore pressure changes and maintaining the time for undrained pore pressure equilibration to within 2 to 3 hours.

Velocity and strain data were recorded after equilibration; however, in soft shales there may still be creep. In M shale, the creep rate was found to be smaller than 10 μStrain/hour. Axial P-wave velocity changes from start of the first load cycle until the end of the last one (at the same stresses and pore pressure) were < 2 m/s for B and D shale, and ≈ 5 m/s (increase) over close to 200 hours for M shale, possibly related to creep or irreversible rock deformation caused by the stress cycles. The observed changes do not indicate any damage of the materials as a result of the stress cycling, but they are not negligible compared to the observed stress sensitivities.

Experimental results: Stress and strain sensitivity

The velocities measured after reaching the target (in situ stress) levels are listed in Table 2. All measured velocities decrease with increasing porosity, as one would expect from generally observed trends (e.g. Holt and Fjær, 2003). The non-saturated T shale should not be compared directly to the others. It is noticed that the ratios between P- and S-wave velocities are much smaller for T shale, which is also what one would expect because of the saturation difference.

Figure 8 shows axial P-wave velocity changes during the undrained load-unload stages for the saturated B, D and M shales, plotted against the stress path parameter κ. The stress sensitivity was calculated as the average over all load and unload stages for each stress path. Figure 9 shows the same plot for the non-saturated T Shale, where the pore pressure was constant (ambient conditions). As can be seen, the stress dependence increases with stress path for all four shales, and within experimental uncertainty also exhibits the anticipated linearity. The actual velocity (v_{Pz}) change recorded after 5 MPa isotropic stress change amounts to a maximum of 12.5 m/s for the saturated shales, and a maximum of 67 m/s for the non-saturated shale, following 6 MPa stress change. The data show that velocity changes, axial strains and pore pressure changes resulting from a loading - unloading cycle are always smaller than the standard deviation, so the average of values obtained during loading and unloading are used for the data points shown in the plots. The stress sensitivity in velocities is found to be typically 10 % larger during unloading than for loading, while the stress path sensitivity $\frac{\Delta S_{Pz}}{\Delta\kappa}$ is typically 30 % larger for loading than for unloading. The main difference is observed for the 1st loading segment, in particular for 3AX and CMS cycling.

Figure 10 shows how the pore pressure changed during the undrained loading stages with B, D and M shales. Again the data points shown are averaged over all load and unload segments within each stress path. The variations of the pore pressures between the segments are within ± 0.1 MPa (2 % of the 5 MPa axial stress change imposed in each step). The measured data do in all cases match perfectly with the linear trend proposed by Skempton (1954) (Eq.(5)). The values of the Skempton parameters are given in Table 3.

Notice that in TI media, the Skempton parameters are part of an invariant 2nd rank tensor with components B_H and B_V. Subscripts H and V refer to horizontal and vertical, i.e. parallel and normal to the symmetry plane of the shale, respectively (Cheng, 1997). The commonly used Skempton parameters A_S and B_S relate to the invariants as:

$$\begin{aligned} B_S &= \frac{B_V + 2B_H}{3} \\ A_S(\theta) &= \frac{B_V\cos^2\theta + B_H\sin^2\theta}{3B_S} \end{aligned} \qquad . \qquad (17)$$

As can be seen, Skempton's A_S depends on the angle θ between the symmetry axis and the maximum principal stress. Measured angular dependence is illustrated in Figure 11 for samples of M Shale with three different orientations.

Drained isotropic loading at the in situ stress level (Figure 7) for M shale gave a stress sensitivity for the axial P-wave of $3.4 \cdot 10^{-3}$ MPa^{-1}. It is interesting to notice that this is close to the value obtained for the non-saturated shale (Figure 9), which is a much stiffer rock with significantly lower porosity. During the constant net stress segment, the axial P-wave velocity for M shale increased with almost 10 m/s as a result of 5 MPa pore and confining pressure (axial and radial stress) increase. This implies that the effective stress controlling the velocity is different from the net stress, and permits estimation of the effective stress coefficient n; in this case $n \approx 0.75$. For the B and D shales, these two segments were performed prior to reaching the in situ stress level. The effective stress coefficients for axial P-wave velocities are included in Table 4 together with the values of the stress sensitivity coefficients A, B and C determined for the axial P-wave on the basis of all different applied stress paths.

Axial strains were recorded throughout the tests, permitting direct measurements of the strain sensitivity parameter R_Pz (Eq. (2)). Figure 12 and Figure 13 show the stress path dependence of the R-parameter for the brine-saturated and the non-saturated shales, respectively. R increases strongly when moving from constant mean stress towards isotropic stress path, reflecting the increase in stiffness depicted in Figure 6. The non-saturated shale, having much lower porosity than the others, also has a much larger stiffness. This makes the strains smaller, and consequently R is 1 to 2 orders of magnitude larger in T shale. For both figures strains were averaged between load and unload segments for each stress path. The data show only minor differences between the individual cycles, for instance the axial strain recorded during the first loading segment is on average 0.02 milliStrain larger than the total average (0.04 milliStrain for the constant mean stress and the triaxial paths). These differences do not play any significant role when evaluating the observed stress path sensitivity of R.

Figure 14 and Figure 15 show examples of the stress path dependence for axial and radial P- and S-wave velocities, based on data for D shale and T shale, respectively. The figures show that all modes exhibit close to linear stress sensitivity. Waves that propagate radially (in the bedding plane) have negative stress sensitivities for the CMS path, because they are influenced by the radial stress, that for this stress path is changed oppositely to the axial stress. Also, the pore pressure increase during axial loading makes the drop in effective radial stress larger and contributes to the negative stress dependence that can be seen in the saturated D shale also for the triaxial stress path (constant confinement). In T Shale, only the radially propagated and polarized S-wave has small negative stress dependence along the triaxial stress path. For uniaxial strain and isotropic loading, the P- and S-waves propagating in the axial direction (normal to bedding) show the largest velocity increase with increasing stress.

IN SITU STRESS PATH DEPENDENCE

In order to apply the laboratory data to time-lapse seismic interpretation, we need to address the stress and pore pressure changes in the overburden caused by depletion (or inflation) of a subsurface reservoir. The in situ stress path is characterized by two parameters, γ_v and γ_h (Hettema et al., 2000):

$$\gamma_\mathrm{v} = \frac{\Delta\sigma_\mathrm{v}}{\Delta p_\mathrm{f(res)}}, \quad \gamma_\mathrm{h} = \frac{\Delta\sigma_\mathrm{h}}{\Delta p_\mathrm{f(res)}} \qquad (18)$$

where σ_v and σ_h are the vertical and horizontal stresses, respectively, while $\Delta p_\mathrm{f(res)}$ refers to the pore pressure change in the reservoir. The parameter γ_v is often termed arching coefficient, as it describes the amount of stress arching around the reservoir. The ratio ($\gamma_\mathrm{h}/\gamma_\mathrm{v}$) between the two coefficients is equivalent to the parameter κ used in the analysis of laboratory data.

According to the linear elastic theory of Geertsma (1973), where there is no elastic contrast between the reservoir and its surroundings, and with a horizontally oriented disk-shaped reservoir, the mean stress is approximately constant everywhere outside the reservoir (see also Fjær et al., 2008; Ch. 12). In this particular case, as can be seen from the definitions in Eq. (18), the overburden stress path coefficients obey the following relationship:

$$\gamma_\mathrm{v} + 2\gamma_\mathrm{h} \approx 0. \qquad (19)$$

The stress path coefficient κ used to describe laboratory experiments corresponds to the ratio $\frac{\gamma_\mathrm{h}}{\gamma_\mathrm{v}}$ in the field, and will hence be approximately -½ from Eq. (19). In reality, the values of the stress path coefficients depend on reservoir geometry and on elastic and non-elastic properties of the reservoir and surrounding formations. Arching is generally promoted by a low aspect ratio (lateral extent over thickness) of the zone where the pore pressure is altered by depletion or inflation. Tilt of the reservoir strongly enhances arching. Furthermore, if the stiffness of the surrounding rocks exceeds that of the reservoir rock, arching is enhanced, while a stiff reservoir in soft surroundings experiences reduced arching. Finally, if the overburden or the reservoir surpasses pure elastic behavior, the stress path changes, whether the deformation is plastic or by formation or activation of faults (Holt et al., 2016); however, analytical models that fully describe the behavior are still lacking.

Numerical techniques give us some insight into overburden stress paths. Figure 16 is derived on the basis of Finite Element (FEM) simulations by Mahi (2003) and Mulders (2003), and demonstrates how the overburden stress path coefficients may change with elastic contrast and reservoir tilt in an idealized case with a disk shaped reservoir in isotropic and linearly elastic rocks. Figure 17 shows the ratio between the stress path coefficients (corresponding to the laboratory stress path parameter κ) as a function of elastic contrast for different degrees of tilt. The figures show that both γ_v and γ_h above the center of a reservoir become positive when the elastic contrast exceeds ≅ 2; meaning that for depletion, both the vertical and horizontal stress will decrease (Morita and Fuh, 2009). This may in practice lead to drilling problems, but it also affects our ability to see 4D time shifts. Notice also that for an elastic contrast < 1, the mean stress will increase when the reservoir depletes, implying that the pore pressure most likely increases (depending on the value of A_S).

The overburden velocity change can be linked to the pore pressure change in the reservoir through the vertical stress change (Eq. (18), so that Eq. (4) becomes:

$$\frac{\Delta \mathrm{v}}{\mathrm{v}} = \gamma_{\mathrm{v}} \left\{ \frac{1+2\kappa}{3} A + (1-\kappa) B - C \frac{\Delta p_f}{\Delta \sigma_z} \right\} \Delta p_{\mathrm{f,res}} \,. \tag{20}$$

To describe the relative velocity change per unit change of reservoir pore pressure in terms of the in situ stress path coefficients and the Skempton parameters we define:

$$P = \frac{\Delta \mathrm{v}}{\mathrm{v} \Delta p_{\mathrm{f,res}}} = \gamma_{\mathrm{v}} \left\{ [\frac{A}{3} + B - A_{\mathrm{S}} B_{\mathrm{S}} C] + [\frac{2A}{3} - B - B_{\mathrm{S}} (1 - A_{\mathrm{S}}) C] \frac{\gamma_{\mathrm{h}}}{\gamma_{\mathrm{v}}} \right\}. \tag{21}$$

Thus; the in situ velocity change increases with increasing depletion, with stress arching (γ_v), and it depends on the pore pressure response in the overburden cf. Eq. (20), and with stress path (γ_h/γ_v (= κ)) cf. Eq. (21).

The in situ R-factor follows from its definition (Eq.(2)) and from Eqs. (10), (17) and (20) (M_v is the relevant stiffness parameter in analogy with the laboratory measured stiffness M_z):

$$
\begin{aligned}
R &= \frac{\Delta \mathrm{v}}{\mathrm{v}\Delta\varepsilon_\mathrm{v}} = \frac{\Delta \mathrm{v}}{\mathrm{v}\Delta p_\mathrm{f,res}}\frac{\Delta p_\mathrm{f,res}}{\Delta\sigma_\mathrm{v}}\frac{\Delta\sigma_\mathrm{v}}{\Delta\varepsilon_\mathrm{v}} = \frac{P}{\gamma_\mathrm{v}}M_\mathrm{v} \\
&= \left\{\left[\frac{A}{3} + B - A_\mathrm{S}B_\mathrm{S}C\right] + \left[\frac{2A}{3} - B - B_\mathrm{S}(1-A_\mathrm{S})C\right]\frac{\gamma_\mathrm{h}}{\gamma_\mathrm{v}}\right\}\left\{\frac{E_\mathrm{V}}{1-(\nu_\mathrm{VH}+\nu_\mathrm{HV})\dfrac{E_\mathrm{V}}{E_\mathrm{H}}\dfrac{\gamma_\mathrm{h}}{\gamma_\mathrm{v}}}\right\} .
\end{aligned}
\qquad (22)
$$

Notice that the E-moduli and Poisson's ratios in the last parenthesis are static moduli.

Figure 18 and Figure 19 show calculated in situ stress sensitivity P and the R parameter, respectively, based on Eq. (20) with rock properties (A, B, C, A_S, B_S) taken from the laboratory experiments with D shale (Table 3 and Table 4). The stress path coefficients derived from FEM simulations as shown in Figure 16 and Figure 17 were used. Both parameters increase with increasing elastic contrast, corresponding to increase in stress path coefficient $\gamma_\mathrm{h}/\gamma_\mathrm{v}$. The values are very low for small or negative contrasts, corresponding to small amounts of stress arching (low γ_v). For large negative contrasts, both the P- and R-factors may become negative, corresponding to impact of increasingly compressive horizontal stresses and possible pore pressure increase in the overburden (upon reservoir depletion). The role of reservoir tilt is very significant in amplifying the stress sensitivity, while R becomes less stress path sensitive and may even be reduced at high elastic contrasts, reflecting the behavior of the ratio $\gamma_\mathrm{h}/\gamma_\mathrm{v}$ as seen in Figure 17.

DISCUSSION

The experiments presented above were performed with three overburden field shale cores brought to in situ stresses and pore pressure, maintaining full saturation, and with a non-saturated shale that was brought in its native state of saturation to effective in situ stresses and no pore pressure. The four shales span porosities from 9 to 36 %, and their clay contents vary from 25 to 76 %. Stresses were altered around the in situ stresses along four different stress paths that span some typical overburden stress changes associated with depletion of or injection into a reservoir below. Laboratory measured ultrasonic velocities show close to linear stress path sensitivity, for all principal P- and S-wave modes that have been measured. This is also what one would expect when stress perturbations are small enough to keep the shale in an elastic state.

The saturated shales were all tested in undrained conditions, which is thought to be representative for the overburden in situ, at least in short term range; i.e. during the lifetime of a depleting reservoir. In the laboratory, the pore pressure response was measured, and shown – in addition to being significant – to follow the linear trend that was proposed by Skempton (1954) for clays. In the field, such pore pressure changes are not measured, but are deemed to exist and will potentially have a significant impact of 4D seismic response. Further, pore pressure changes along with stress changes in the overburden will have impact on operational aspects like stability during drilling of infill wells.

The values of the Skempton-parameters depend on the drained, solid grain and pore fluid stiffnesses, in addition to anisotropy and plasticity. The B_S will be close to 1 for soft shale or clay where the drained bulk modulus is negligible compared to that of the pore fluid, and close to 0 if the pore fluid is gas. In the latter case, because of the high gas compressibility, the pore pressure change is negligible, and the response is equivalent to that of a drained scenario.

In order to perform a sensitivity analysis, we assume that the overburden above a monitored reservoir consists of shale with the same properties as the M shale that was studied experimentally. The stress arching coefficient γ_v is somewhat arbitrarily set to 0.1. We analyze only changes in the vertical P-wave velocity (Δv_{pv}), assuming undrained response and fully saturated overburden. Figure 21 shows that the sensitivity of the vertical P-wave velocity to the reservoir pore pressure change (P_{PV}) increases with decreasing B_S for all stress paths. It should be noted that the reduced P-values compared to the laboratory measured stress sensitivity (S_{Pz}) (Figure 8) is caused by the multiplication factor γ_V in Eq.(21). Figure 22 shows the corresponding R-factor, calculated from Eq. (22). The *R*-factor is seen to increase strongly with all stress paths as a result of decreasing B_S.

The influence of A_S on in situ sensitivity of vertical P-wave velocity to reservoir pore pressure (P_{PV}) is illustrated in Figure 22, while its influence on the *R*-parameter is shown in Figure 23. As expected A_S has no influence for an isotropic stress path, but decreasing A_S leads to strongly increased stress sensitivity and *R*-factor for lower values of the stress path expressed by γ_h/γ_V. Notice that the value of A_S may vary widely. From our work, it is clearly linked to the degree of anisotropy, and to the orientation of principal stress with respect to bedding. For larger stress increments beyond the elastic regime, plasticity will also impact on the value of A_S.

We observe two to three times higher stress sensitivity in the non-saturated shale, where we probe the drained behaviour of the rock, compared to the undrained saturated shales. But, as can be seen from Table 4, the coefficients A_{Pz} and B_{Pz} controlling the axial P-wave stress sensitivity in drained conditions are surprisingly similar for all 4 shales. This means that the Skempton parameters controlling pore pressure evolution, and the C_{Pz} parameter controlling the effective stress for velocities (Eq.(3)), are important rock properties required in order to estimate in situ stress sensitivity. Another implication is that if the overburden is monitored over several decades (e.g. monitoring of CO_2 sequestration or long term integrity of abandoned production sites), the overburden response turns towards drained behaviour as pore pressure will equilibrate towards reservoir pressure. This will lead to a measurable 4D response caused by effective stress changes and associated porosity alteration.

The stress history of a rock core is different from that of the same rock in situ. It is well-known in soil and rock mechanics (Atkinson and Bransby, 1977) that the mechanical behaviour during initial loading is much softer (normally consolidated) than during unloading or repeated loading below the previously experienced stress (overconsolidated). Rocks appear to remember the previously most damaging stress state, which might also have been imposed during coring (Holt et al., 2000), contributing further to the difference between in situ and laboratory measurements. One would expect stress sensitivity to be larger in a normal consolidation situation than for overconsolidated rocks. Probing different stress paths in normal consolidation starting from the same stress state is not possible on the same core. Our data are as such more representative of overconsolidated behaviour, which might be the case in situ as well when the present stress state is lower than any paleo-stress. The data shown here indicate minor effects of damaging the rocks during stress cycling in the laboratory.

Linear stress path dependence may be predicted by several models (Prioul et al., 2004; Sayers, 2006; Fjær, 2006); however, the challenge is to capture in a quantitative manner the impact of pore pressure and the full anisotropy. As mentioned above, the approach by Prioul et al. (2004) is similar to the linearized stress dependence suggested in Eq.(3); however, the assumption of isotropic nonlinearity (limiting the number of nonlinearity parameters to three) appears to be an oversimplification, preventing a good match to the overall stress path sensitivity for different P- and S-modes.

Translating the laboratory results to the field requires knowledge of the stress path, presumably from geomechanical simulations, or aided by in situ strain measurements. As shown by Figure 18 and Figure 19, stress path, reservoir geometry, and tilt are primary factors in control of in situ stress and strain sensitivity. Obviously, the aspect ratio of the depleting (or inflated) reservoir zone plays an equally important role: Decreasing the aspect ratio will lead to more arching and hence more stress sensitivity. In the analysis performed here, the overburden properties were taken as those of a relatively soft shale (D shale). Notice that the elastic contrast relevant here is the contrast between the undrained overburden and the drained reservoir rock. In case of a stiffer overburden, the *R*-factor in particular would have been boosted, because the vertical strain would be reduced. In fact, the stress path (which partly controls the vertical strain) seems to be the main factor controlling *R*, which means that in situ stress path characterization from 4D seismic may be a possible opportunity.

This paper only shows ultrasonic data. Similar experiments are being performed in the seismic frequency range, but more work is required before completed data sets are available. In Holt et al. (2016) an example was given, showing simultaneous measurement of stress sensitivity at ultrasonic and seismic frequencies in a partially saturated sample of Pierre Shale. The data showed larger stress path sensitivity of the axial P-wave from the low frequency data, and also larger absolute stress sensitivity for all stress paths except constant mean stress. Sorting out the role of frequency dependence is very important in order improve our ability to translate laboratory experience into valid field data interpretation procedures.

CONCLUSIONS

The stress dependence and in particular the strain dependence of wave velocities in shales have been found to depend on the stress path. For undrained stress changes of a few MPa around an elevated stress state, representative of in situ stress and pore pressure, laboratory measured stress sensitivities of ultrasonic P- and S-wave velocities in principal directions exhibit linear trends with stress path (stress path in the laboratory is defined as the incremental change in radial stress vs. axial stress). The undrained pore pressure response is also linear in stress path, in agreement with the Skempton hypothesis adapted from soil mechanics. The stress sensitivity is much smaller in undrained than drained conditions, and the role of pore pressure change appears very significant. To our knowledge, this is the first well documented observation of stress path sensitivity in shales. Similar trends have been deduced from laboratory data with other rock types, and are also inherent in a few existing rock physics theories.

A linear relationship between in situ velocity changes in overburden shale and pore pressure depletion or inflation in an underlying reservoir or storage site beneath has been derived, and enables estimation of changes in 4D seismic travel time changes (e.g. through the dilation parameter R) or reflectivities. Required input is velocity measurements along different relevant stress paths in the laboratory, and knowledge of in situ stress path characteristics (defined through changes in horizontal and vertical stresses with reservoir pore pressure, i.e. γ_h and γ_v) from geomechanical modeling. Determination of depth dependent R-factor may alternatively enable quantification of in situ stress and pore pressure changes, being of high relevance for safe and stable future drilling operations.

ACKNOWLEDGEMENTS

The author acknowledges the financial support through the Joint Industry Project "Shale Rock Physics" at SINTEF Petroleum Research, funded by The Research Council of Norway through the PETROMAKS 2 Program (Research Council Grant #: 234074) and the participating companies BP, DONG Energy, Engie, Maersk and Total. The Research Council of Norway through the PETROMAKS 2 Program and a number of companies sponsoring the ROSE program ("Geophysical methods for subsurface imaging and monitoring"; Research Council Grant #: 228400) at NTNU are also acknowledged. Several discussions with colleagues at SINTEF and NTNU have contributed to the contents of this Paper, particularly mentioned are Erling Fjær with SINTEF and Kenneth Duffaut at NTNU.

REFERENCES

Atkinson, J.H. and P.L. Bransby, 1977, *The Mechanics of Soils: An Introduction to Critical State Soil Mechanics*. McGraw-Hill, 375 pp.

Cheng, A. H.-D., 1997, Material coefficients of anisotropic poroelasticity: Int. J. Rock Mech. & Min. Sci. 34, 199-205.

Cruts, H.M.A., J. Groenenboom, A.J.W. Duijndam, J.T. Fokkema, 1995, Experimental verification of stress-induced anisotropy: 65th Ann. Int. Mtg. SEG, Expanded Abstracts, 894-897.

De Gennaro, S., A. Onaisi, A. Grandi, L- Ben-Brahim, V. Neillo, 2008, 4D reservoir geomechanics: a case study from the HP/HT reservoirs of the Elgin and Franklin fields: First Break, **26**, 53-59.

Domnesteanu, P., C. McCann, J. Sothcott, 2002, Velocity anisotropy and attenuation of shale in under- and overpressured conditions: Geophys. Prospecting, **50**, 487-503.

Dewhurst, D.N. and A.F- Siggins, 2006, Impact of fabric, microcracks and stress field on shale anisotropy: Geophys. J. Int., **165**, 135–148.

Dillen, M.W.P., H.M.A. Cruts, J. Groenenboom, J.T. Fokkema, A.J.W.Duijndam, 1999, Ultrasonic velocity and shear-wave splitting behavior of a Colton sandstone under a changing triaxial stress: Geophysics **64**, 1603-1607.

Fjær, E., 2006, Modeling the stress dependence of wave velocities in soft rocks: ARMA 06-1070; 8 pp.

Fjær, E., R.M. Holt, P. Horsrud, A.M. Raaen, R. Risnes, 2008, Petroleum Related Rock Mechanics: Elsevier; 491 pp.

Geertsma, J., 1973, A basic theory of subsidence due to reservoir compaction: The homogeneous case: Verhandelingen Kon. Ned. Geol. Mijnbouwk. Gen. **28**, 43-62

Hatchell, P. and S. Bourne, 2005, Rocks under strain: Strain-induced time-lapse time shifts are observed for depleting reservoirs: The Leading Edge **24**, 1222-1225.

Holt, R.M., M. Brignoli, C.J. Kenter, 2000, Core quality: quantification of coring-induced rock alteration: Int. J. Rock Mech. & Min. Sci. **37**, 889-907

Holt, R.M. and E. Fjær, 2003, Wave velocities in shales – a rock physics model: EAGE 65th Conf., Stavanger, Norway 2-5 June 2003; 4 pp.

Holt, R.M., E. Fjær, O.-M. Nes, J.F.Stenebråten, 2008, Strain sensitivity of wave velocities in sediments and sedimentary rocks: ARMA 08-291; 8 pp.

Holt, R.M. and E. Fjær, 2009, R – From laboratory data to 4D seismic interpretation: 79th Ann. Int. Mtg. SEG Expanded Abstracts; 4 pp.

Holt, R.M. and J.F. Stenebråten, 2013, Controlled laboratory experiments to assess the geomechanical influence of subsurface injection and depletion processes on 4D seismic responses: Geophys. Prospecting **61**, 476-488; doi: 10.1111/1365-2478.12040

Holt, R.M., A. Bauer, E. Fjær, J.F. Stenebråten, D. Szewczyk, P. Horsrud, 2015, Relating static and dynamic mechanical anisotropies of shale: ARMA 15-484; 7 pp.

Holt, R.M., S. Gheibi, A. Lavrov, 2016, Where does the stress path lead? Irreversibility and hysteresis in reservoir geomechanics: ARMA 16-496; 12 pp.

Holt, R.M., A. Bauer, A. Bakk, D. Szewczyk, 2016, Stress path dependence of ultrasonic and seismic velocities in shale: SEG Expanded Abstract; SEG Ann. Int. Tech. Conf., Dallas, Tx; 4 pp.

Hornby, B.E., 1998, Experimental laboratory determination of the dynamic elastic properties of wet, drained shales: J. Geophys. Res., **103**, B12, 29945-29964.

Horsrud, P., E.F. Sønstebø, R. Bøe, 1998, Mechanical and petrophysical properties of North Sea shales: Int. J. Rock Mech. & Min. Sci. **35**, 1009-1020.

Johnston, D.H., 1987, Physical properties of shale at temperature and pressure: Geophysics **52**, 1391-1401. doi: 10.1190/1.1442251

Johnston, J.E. and N.I. Christensen, 1995, Seismic anisotropy of shales: J. Geophys. Res. **100**, 5991-6003.

Kenter, C.J., A.v.d. Beukel, P. Hatchell, K. Maron, M. Molenaar, 2004, Evaluation of reservoir characteristics from timeshifts in the overburden: ARMA/NARMS 04-627, 8 pp.

Mahi, A., 2003, Stress Path of Depleting Reservoirs: MSc Thesis, NTNU, Norway

Morita, N., G.-F. Fuh, 2009, Parametric analysis of stress reduction in the cap rock above compacting reservoirs: SPE Drilling & Completion **24**, 659-670, doi: 10.2118/114629-PA

Mulders, F.M.M., 2003, Modelling of stress development and fault slip in and around a producing gas reservoir: PhD Thesis, TU Delft, Netherlands

Pervukhina, M., D. Dewhurst, B. Gurevich, U. Kuila, T. Siggins, M. Raven, H.M.N. Bolås, 2008, Stress-dependent elastic properties of shales: measurement and modeling: The Leading Edge **27**, 772-779. doi: 10.1190/1.2944162

Prioul, R., A. Bakulin, V. Bakulin, 2004, Nonlinear rock physics model for estimation of 3D subsurface stress in anisotropic formations: Theory and laboratory verification: Geophysics, 69, 415-425. doi: 10.1190/1.1707061

Røste, T., A. Stovas, M. Landrø, 2006, Estimation of layer thickness and velocity changes using 4D prestack seismic data: Geophysics **71**, S219 - S234.

Røste, T., G. Ke, 2017, Overburden time shifts – Indicating undrained areas and fault transmissibility in the reservoir: The Leading Edge **36**, 308-315.

Sayers, C.M., 2006, Sensitivity of time-lapse seismic to reservoir stress path: Geophys. Prospecting **54**, 369-380.

Scott, T.E., 2007, The effects of stress paths on acoustic velocities and 4D seismic imaging: The Leading Edge **26**, 602-608.

Skempton, A.W.,1954, The pore-pressure coefficients *A* and *B*: Géotechnique **4**, 143-147. http://dx.doi.org/10.1680/geot.1954.4.4.143.

Wang, Z., 2002, Seismic anisotropy in sedimentary rocks, part 2: Laboratory data: Geophysics 67, 1423-1440. doi: 10.1190/1.1512743

FIGURE CAPTIONS

Figure 1	Stress sensitivity of the P-wave velocity normal to bedding from isotropic tests published in the literature (Johnston, 1987; Johnston and Christensen, 1995; Hornby; 1998; Wang, 2002; Domnesteanu et al., 2002, Pervukhina et al., 2008). The lines represent the intervals of net stress (confining pressure (= radial stress) minus pore pressure) across which stress sensitivities are estimated. Note that velocity vs. stress was close to linear over all these segments. Stress sensitivity is defined as the relative change in axial P-wave velocity vs. change in axial stress.
Figure 2	Axial stress, radial stress (confining pressure) and pore pressure during laboratory test with brine saturated kaolinite. The test was done in drained conditions, except for the CMS segments during days 12-14.
Figure 3	Axial P-wave velocity data from three different stress paths with a compacted kaolinite-brine mixture; normalised to the initial value for each stress path segment. The strain sensitivities (*R*-values) found were 2.6 during undrained CMS with axial unloading, and 1.7 during axial CMS reloading below the previous stress state, crossing over to ~ 0 above, where the material yielded plastically. During drained uniaxial compaction (K_0), R was 1.8, whereas R was 7.2 during initial drained isotropic loading, increasing to 9.3 and 9.1 during isotropic unloading and reloading, respectively.
Figure 4	Stress sensitivity of the P-wave propagating in axial direction (z) vs. stress path in the experiments with dry Colton sandstone, shown by Dillen et al. (1999).The tests were done in a true triaxial set-up, with stresses $\sigma_x = \sigma_y$.
Figure 5	Relative change of P- and S-wave velocities with stress path, based on the simulated behavior of P- and S-wave stress sensitivities for a sandstone along different stress paths. The graph is produced on basis of Figure 12 in Sayers (2006), representing a sandstone.
Figure 6	Illustration of stress path sensitivity of the *R*-parameter for a fictitious case where the stress dependence $(\Delta v_{Pz})/v_{Pz}\Delta\sigma_z)$ in Eq. (11) is constant = 10^{-3} MPa^{-1}. The calculation is based on the isotropic case (cfr. Eq, (12) with Young's

modulus = 5 GPa and Poisson's ratio = 0.30. The curve then simply shows the stiffness $\Delta\sigma_z/\Delta\varepsilon_z$ vs. stress path.

Figure 7 Drained isotropic, constant net stress, and undrained stress isotropic, uniaxial stress, uniaxial strain and constant mean stress cycles performed starting from the in situ stress and pore pressure in M Shale.

Figure 8 Stress sensitivity of the ultrasonic P-wave velocity parallel to the symmetry axis (normal to bedding) for three brine-saturated field shales, plotted a versus stress path (κ, cf. Eq. (1)) for incremental constant mean stress, triaxial, uniaxial strain and isotropic loading and unloading.

Figure 9 Stress sensitivity of the ultrasonic P-wave velocity parallel to the symmetry axis (normal to bedding) for the non-saturated shale (T Shale), plotted a versus stress path (κ, cf. Eq. (1)) for incremental isostaic stress, triaxial, uniaxial strain and isotropic loading and unloading.

Figure 10 Pore pressure evolution in the three brine-saturated shales plotted against stress path path for incremental constant mean stress, triaxial, uniaxial strain and isotropic loading and unloading. The axial stress change was 5 MPa for all stress path stages.

Figure 11 Change in Skempton's A_S parameter vs. inclination (angle between the sample axis and the symmetry axis) for laboratory tests with three differently oriented core plugs from M Shale. The curve is drawn according to Eq. (17) on the basis of A_S and B_S obtained from a core with zero inclination (M shale in Figure 10 and Table 3).

Figure 12 Strain sensitivity of the ultrasonic P-wave velocity parallel to the symmetry axis (normal to bedding) for three brine-saturated (B, D and M) shales, plotted a versus stress path for incremental isotropic stress, triaxial, uniaxial strain and isotropic stress (average of loading and unloading).

Figure 13 Strain sensitivity of the ultrasonic P-wave velocity parallel to the symmetry axis (normal to bedding) for the non-saturate (T) shale, plotted a versus stress path for incremental constant mean stress, triaxial, uniaxial strain and isotropic stress (average of loading and unloading).

Figure 14	Stress sensitivity of ultrasonic P- and S-wave velocities parallel and normal to the symmetry axis (normal to bedding) for brine-saturated D shale, plotted a versus stress path for incremental constant mean stress, triaxial, uniaxial strain and isotropic (average of loading and unloading). Best linear fits to the data are shown as solid lines for P-waves (bold for the axial P-wave; Pz), and as dashed lines for S-waves (bold for axial S-wave, Sz).
Figure 15	Stress sensitivity of ultrasonic P- and S-wave velocities parallel and normal to the symmetry axis (normal to bedding) for non-saturated T shale, plotted a versus stress path for incremental constant mean stress, triaxial, uniaxial strain and isotropic (average of loading and unloading). Best linear fits to the data are shown as solid lines for P-waves (bold for the axial P-wave; Pz), and as dashed lines for S-waves (bold for axial S-wave, Sz).
Figure 16	The stress path coefficients γ_v and γ_h at top center above a reservoir plotted versus elastic contrast between the reservoir and its surroundings (notice the logarithmic scale), for cases of reservoir tilt from 0 to 15°. The curves are based on empirical relationships derived from 2D FEM simulations (Mahi, 2003; Mulder, 2003). The reservoir is placed at 3000 m depth and has an aspect ratio of 0.1. Poisson's ratio was assumed to be the same everywhere, and set = 0.30.
Figure 17	The ratio γ_h / γ_v at top center above a reservoir vs. elastic contrast (logarithmic scale) demonstrating the effect of reservoir tilt on the overburden stress path. The curves are based on empirical relationships derived from 2D FEM simulations (Mahi, 2003; Mulder, 2003). The reservoir is placed at 3000 m depth and has an aspect ratio of 0.1. Poisson's ratio was assumed to be the same everywhere, and set = 0.30.
Figure 18	Calculated in situ dependence of vertical P-wave velocity with respect to reservoir pore pressure change, using laboratory measured stress sensitivity and Skempton parameters for D shale; plotted against elastic contrast between surrounding (overburden) and reservoir rocks for 0 and 10° reservoir tilt, based on the 2D FEM simulations shown in Figure 16 and Figure 17, using Eq. (21).
Figure 19	Calculated *R*-parameter, using laboratory measured stress sensitivity and Skempton parameters for D shale, plotted against elastic contrast between

surrounding (overburden) and reservoir rocks for 0 and 10° reservoir tilt, based on the 2D FEM simulations shown in Figure 16 and Figure 17, using Eq. (22).

Figure 20 In situ sensitivity of vertical P-wave velocity to reservoir pore pressure change (P_{PV}, cfr Eq.(21)) vs. in situ stress path for three different values of Skempton's B_{S} (A_{S} = 0.53). Ultrasonic stress sensitivity parameters are used (see text); $\gamma_{\mathrm{v}} = 0.1$.

Figure 21 In situ R-parameter for vertical P-wave velocity (cfr Eq.(22)) vs. in situ stress path for three different values of Skempton's B_{S} (A_{S} = 0.53). Ultrasonic stress sensitivity parameters are used (see text).

Figure 22 In situ sensitivity of vertical P-wave velocity to reservoir pore pressure change (P_{PV}, cf. Eq.(21)) vs. in situ stress path for three different values of Skempton's A_{S} (B_{S} = 0.87). Ultrasonic stress sensitivity parameters are used (see text); γ_{v} = 0.1.

Figure 23 In situ R-parameter (cf. Eq.(22)) vs. in situ stress path for three different values of Skempton's A_{S} (B_{S} = 0.87). Ultrasonic stress sensitivity parameters are used (see text).

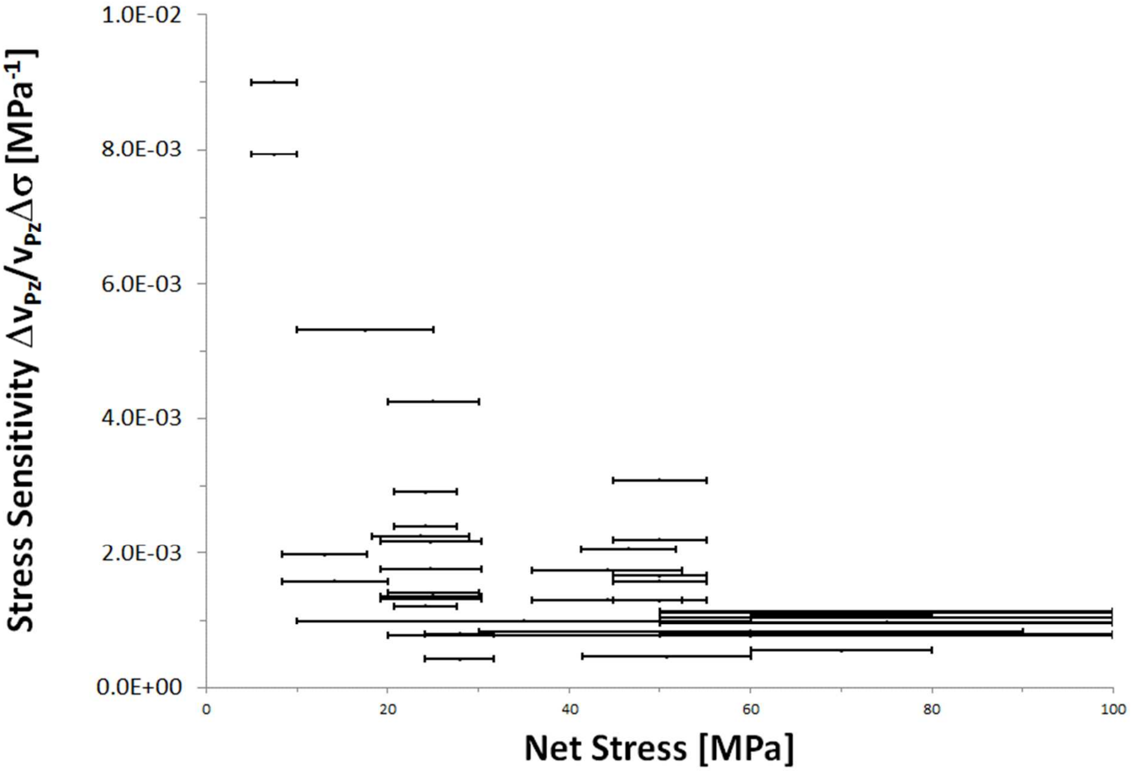
Stress Sensitivity $\Delta v_{Pz}/v_{Pz}\Delta\sigma$ [MPa^{-1}]
1.0E-02
8.0E-03
6.0E-03
4.0E-03
2.0E-03
0.0E+00
0
20
40
60
80
100
Net Stress [MPa]

Figure 1

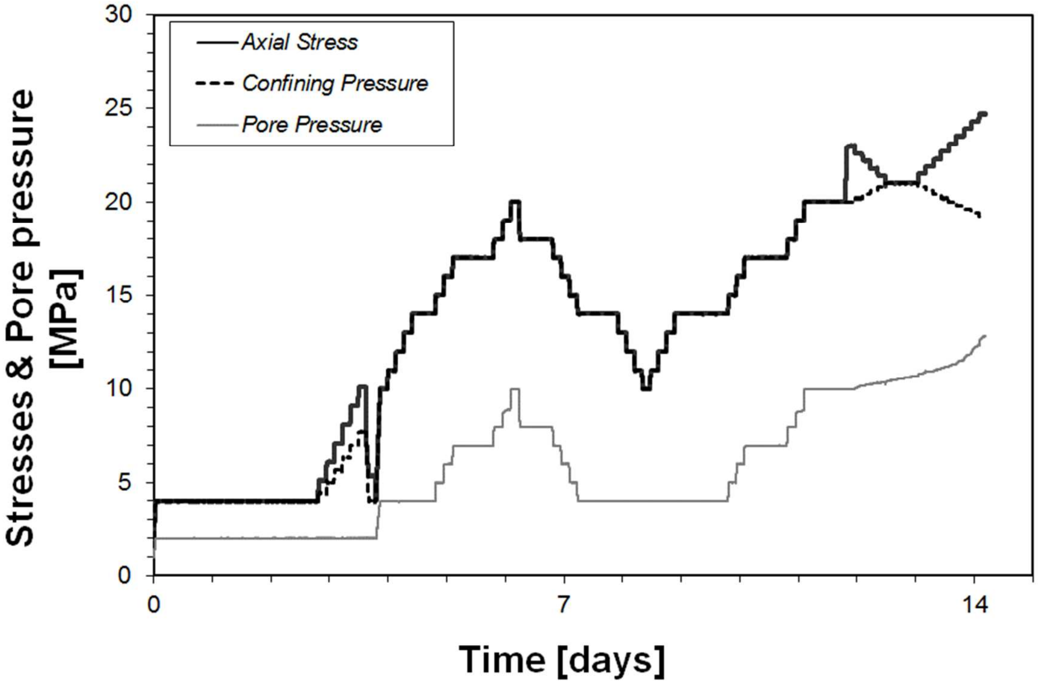
Axial Stress
Confining Pressure
Pore Pressure
Stresses & Pore pressure [MPa]
0
5
10
15
20
25
30
Time [days]
0
7
14

Figure 2

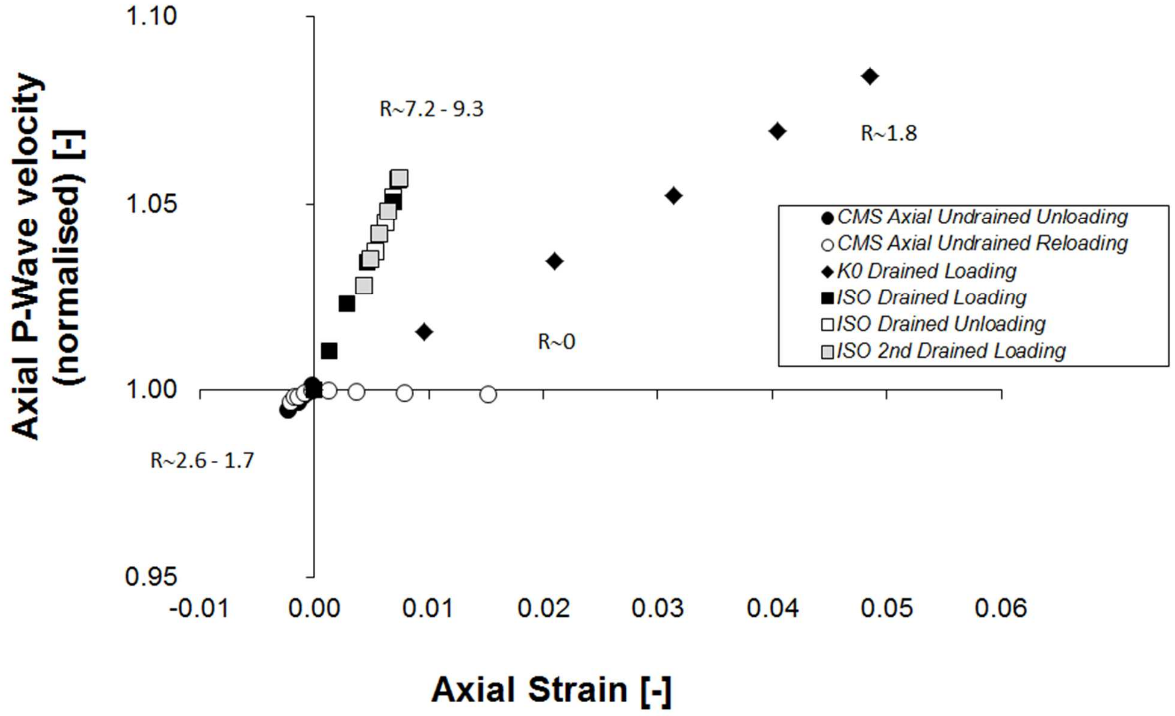
1.10
1.05
1.00
0.95
-0.01
0.00
0.01
0.02
0.03
0.04
0.05
0.06
Axial P-Wave velocity (normalised) [-]
Axial Strain [-]
R~7.2 - 9.3
R~1.8
R~0
R~2.6 - 1.7
● CMS Axial Undrained Unloading
○ CMS Axial Undrained Reloading
◆ K0 Drained Loading
■ ISO Drained Loading
□ ISO Drained Unloading
▨ ISO 2nd Drained Loading

Figure 3

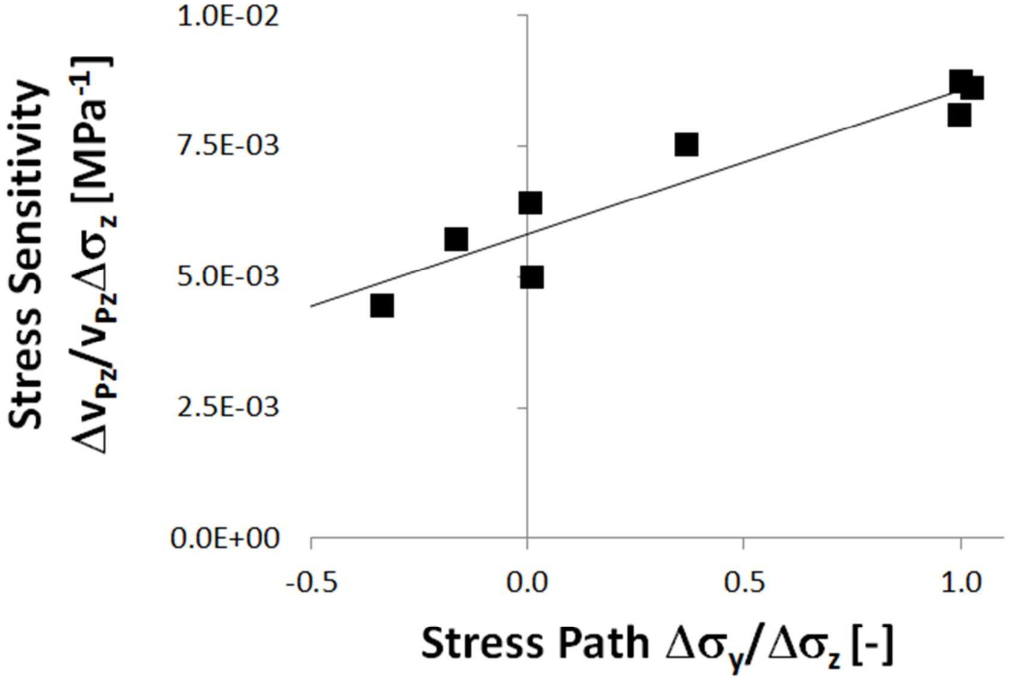
1.0E-02
7.5E-03
5.0E-03
2.5E-03
0.0E+00
-0.5
0.0
0.5
1.0
Stress Sensitivity
$\Delta v_{Pz}/v_{Pz}\Delta\sigma_z$ [MPa^{-1}]
Stress Path $\Delta\sigma_y/\Delta\sigma_z$ [-]

Figure 4

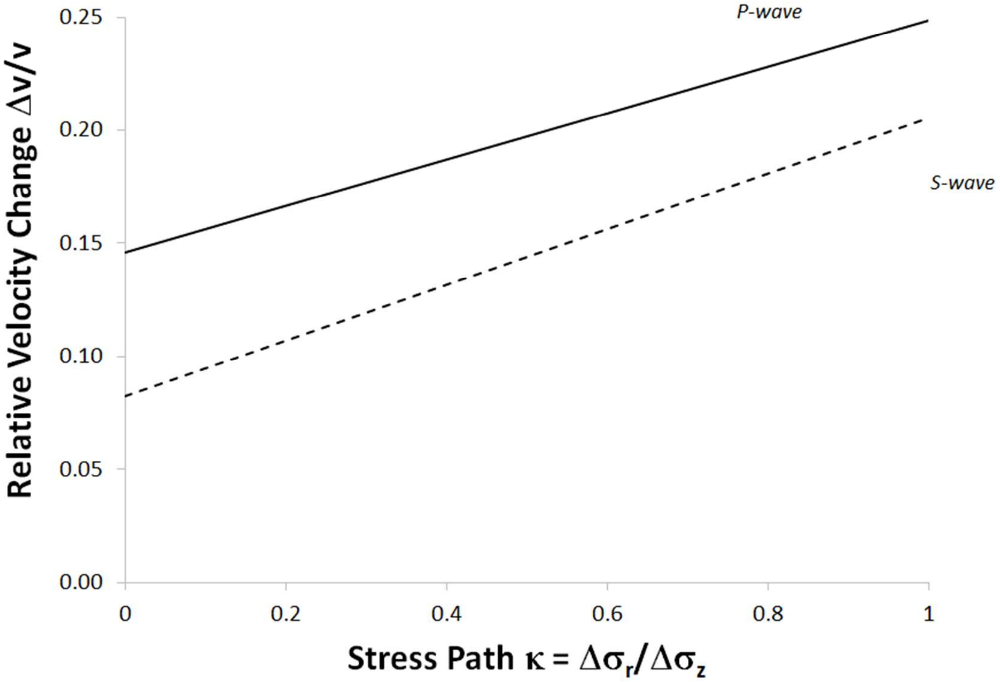
Relative Velocity Change $\Delta v/v$
0.25
0.20
0.15
0.10
0.05
0.00
0
0.2
0.4
0.6
0.8
1
Stress Path $\kappa = \Delta\sigma_r/\Delta\sigma_z$
P-wave
S-wave

Figure 5

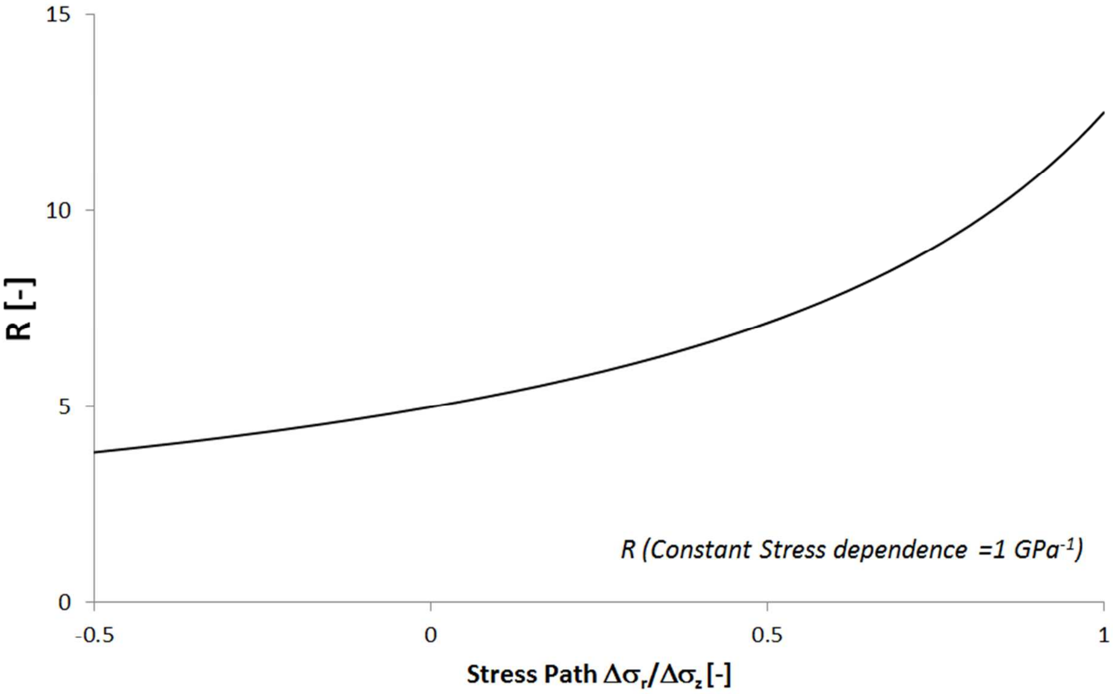
15
10
5
0
R [-]
-0.5
0
0.5
1
Stress Path Δσr/Δσz [-]
R (Constant Stress dependence =1 GPa-1)

Figure 6

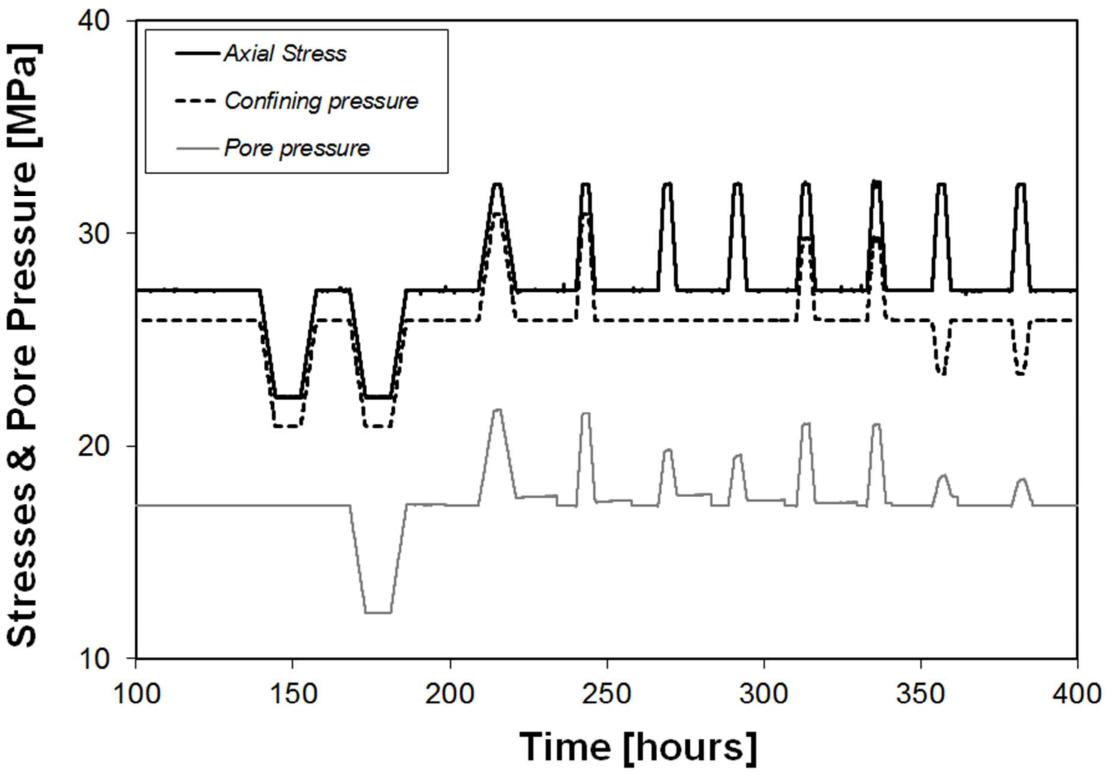
40
30
20
10
Stresses & Pore Pressure [MPa]
100
150
200
250
300
350
400
Time [hours]
Axial Stress
Confining pressure
Pore pressure

Figure 7

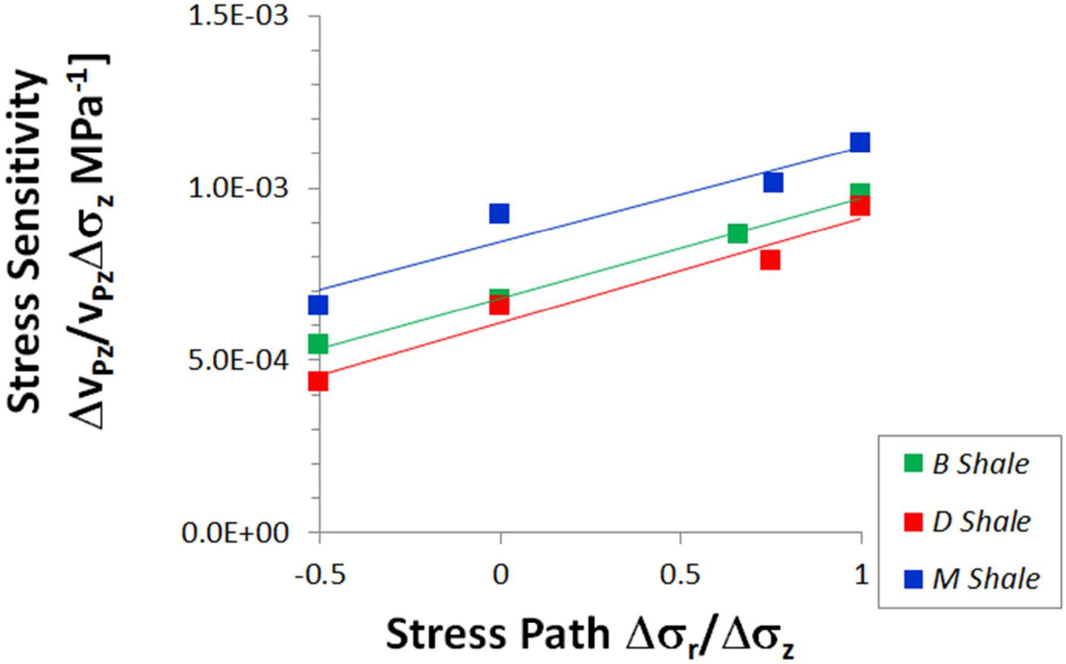

1.5E-03
1.0E-03
5.0E-04
0.0E+00
-0.5
0
0.5
1
Stress Sensitivity
$\Delta v_{Pz}/v_{Pz}\Delta\sigma_z$ MPa^{-1}]
Stress Path $\Delta\sigma_r/\Delta\sigma_z$
B Shale
D Shale
M Shale

Figure 8

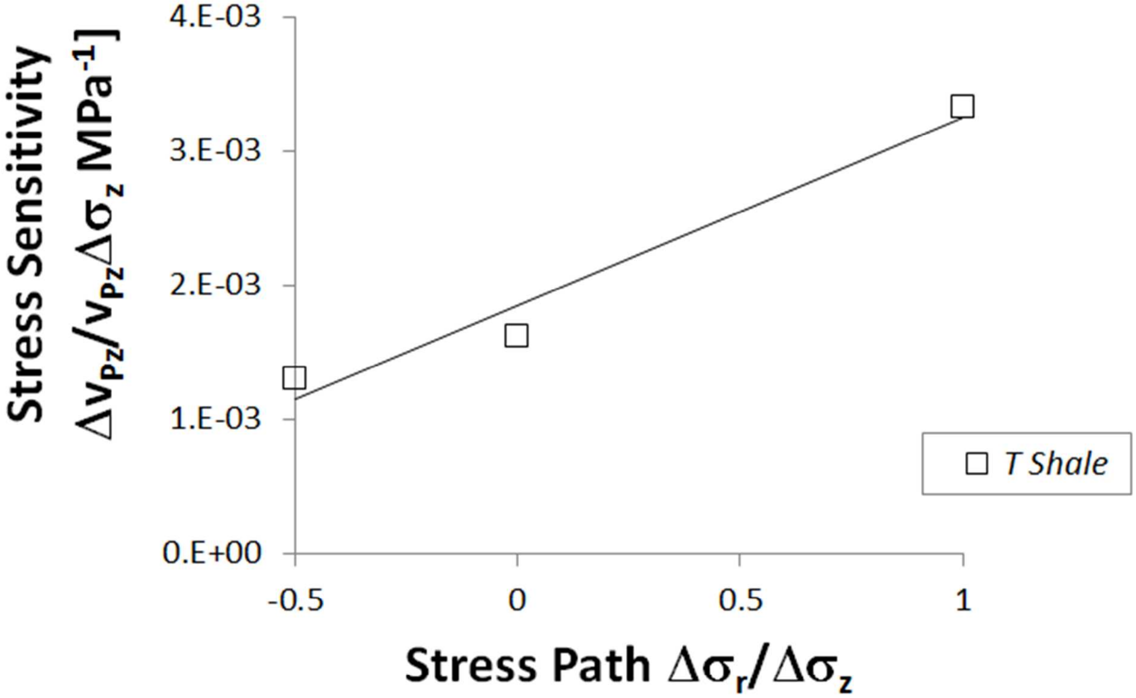
Stress Sensitivity
$\Delta v_{Pz}/v_{Pz}\Delta\sigma_z$ MPa^{-1}]
4.E-03
3.E-03
2.E-03
1.E-03
0.E+00
-0.5
0
0.5
1
Stress Path $\Delta\sigma_r/\Delta\sigma_z$
□ T Shale

Figure 9

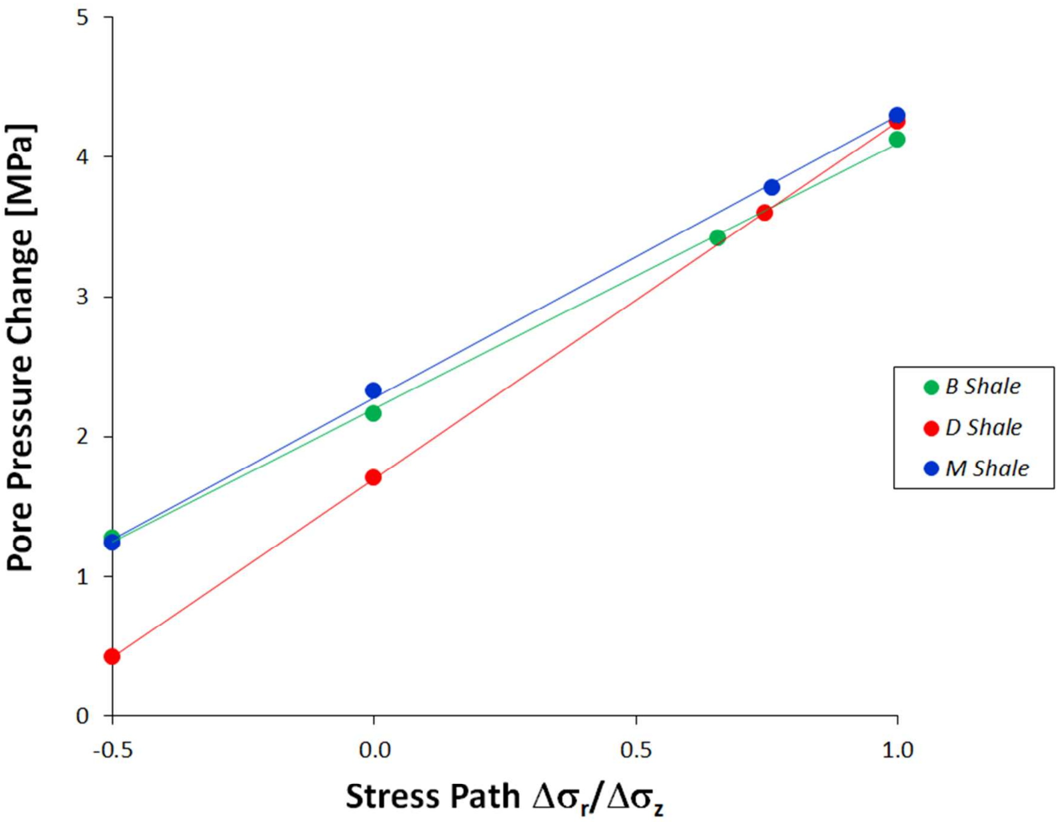
5
4
3
2
1
0
Pore Pressure Change [MPa]
-0.5
0.0
0.5
1.0
Stress Path $\Delta\sigma_r/\Delta\sigma_z$
B Shale
D Shale
M Shale

Figure 10 .

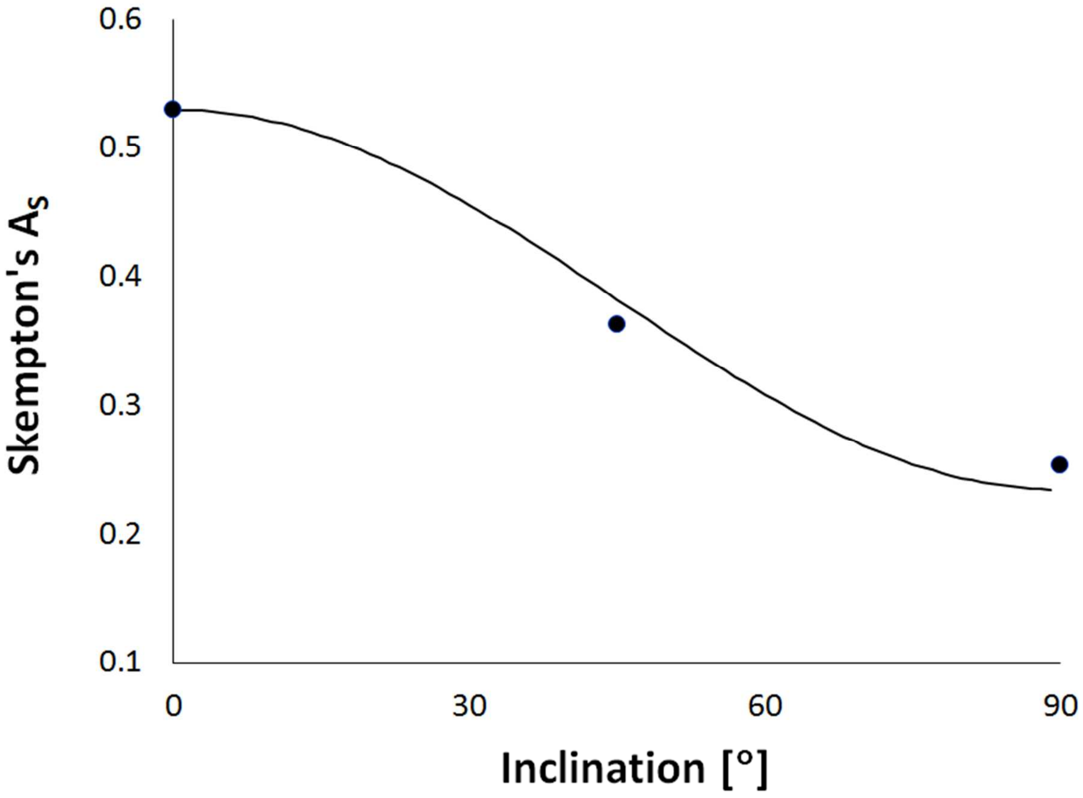

Figure 11

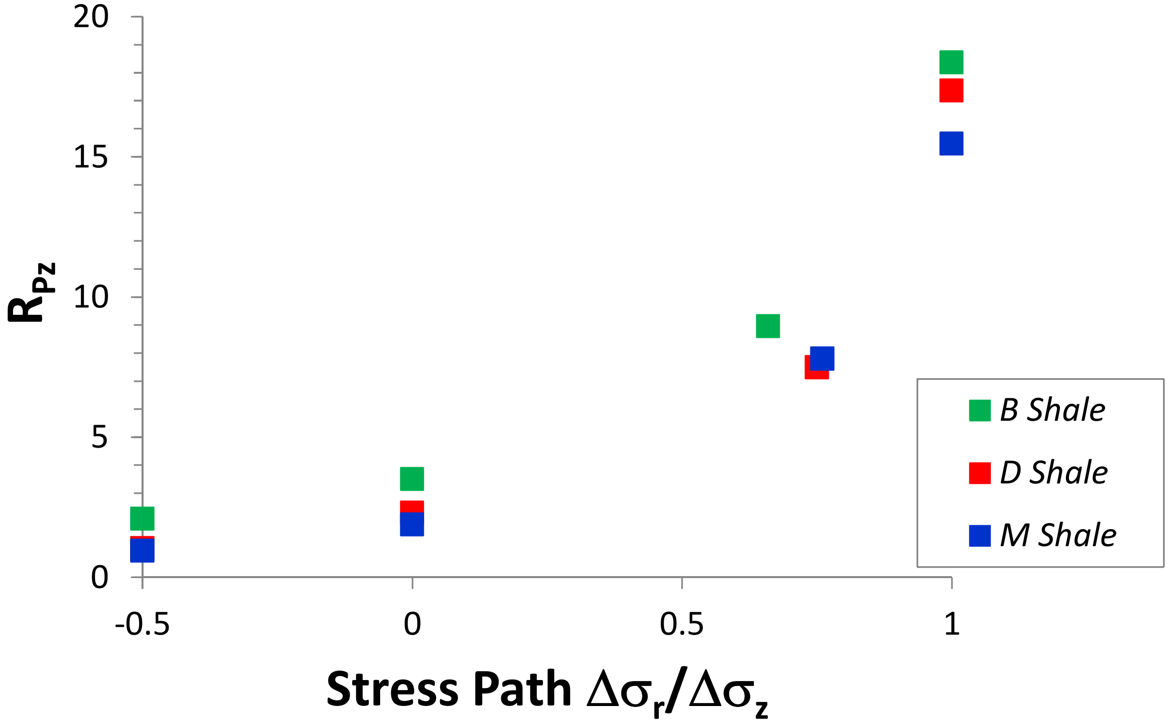
20
15
10
5
0
R_{Pz}
-0.5
0
0.5
1
Stress Path $\Delta\sigma_r/\Delta\sigma_z$
B Shale
D Shale
M Shale

Figure 12

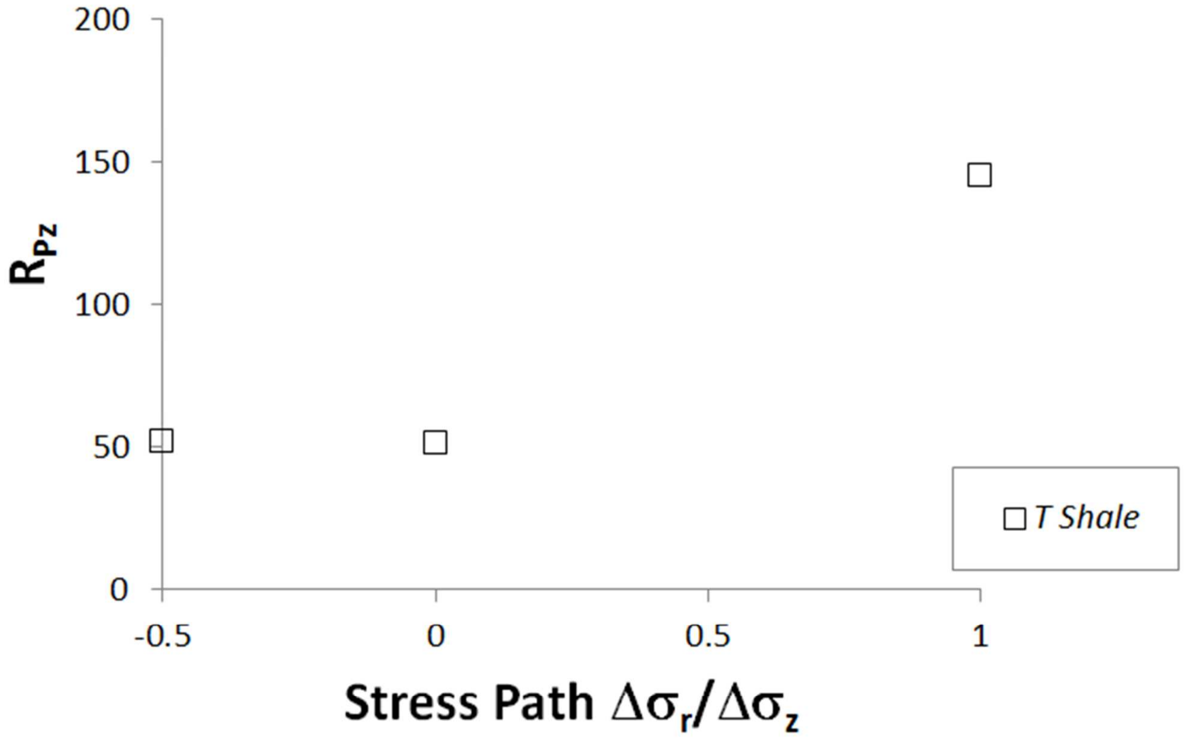
200
150
100
50
0
R_{Pz}
-0.5
0
0.5
1
Stress Path $\Delta\sigma_r/\Delta\sigma_z$
□ T Shale

Figure 13

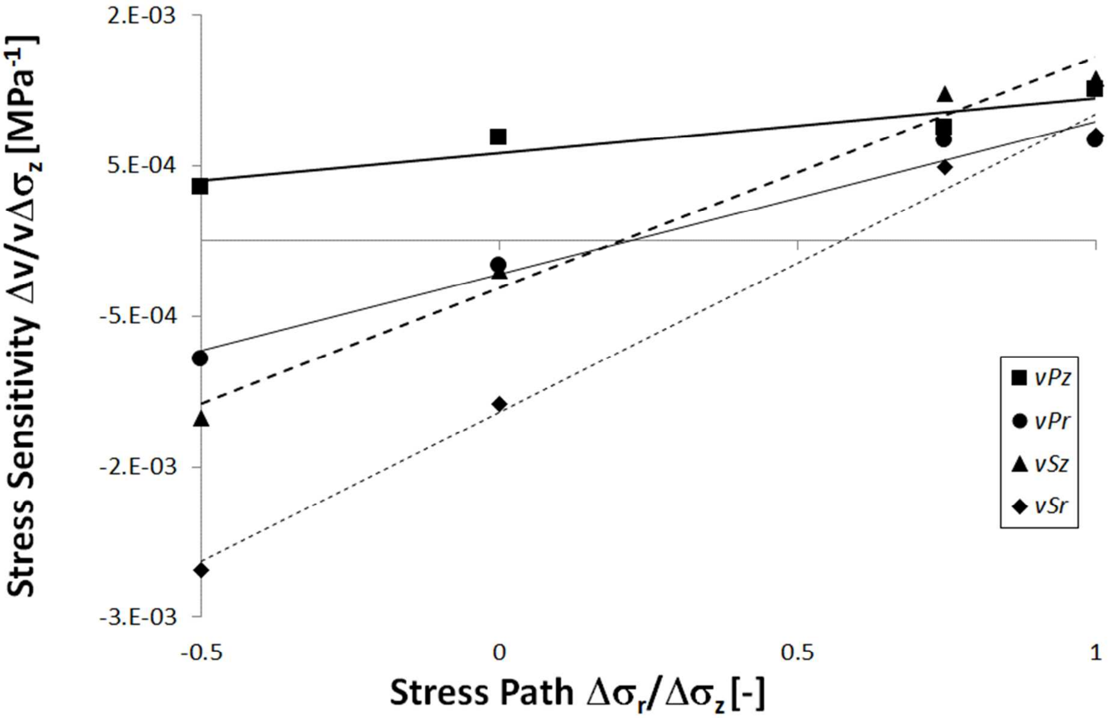
Stress Sensitivity $\Delta v/v\Delta\sigma_z$ [MPa^{-1}]
2.E-03
5.E-04
-5.E-04
-2.E-03
-3.E-03
-0.5
0
0.5
1
Stress Path $\Delta\sigma_r/\Delta\sigma_z$ [-]
■ vPz
● vPr
▲ vSz
◆ vSr

Figure 14

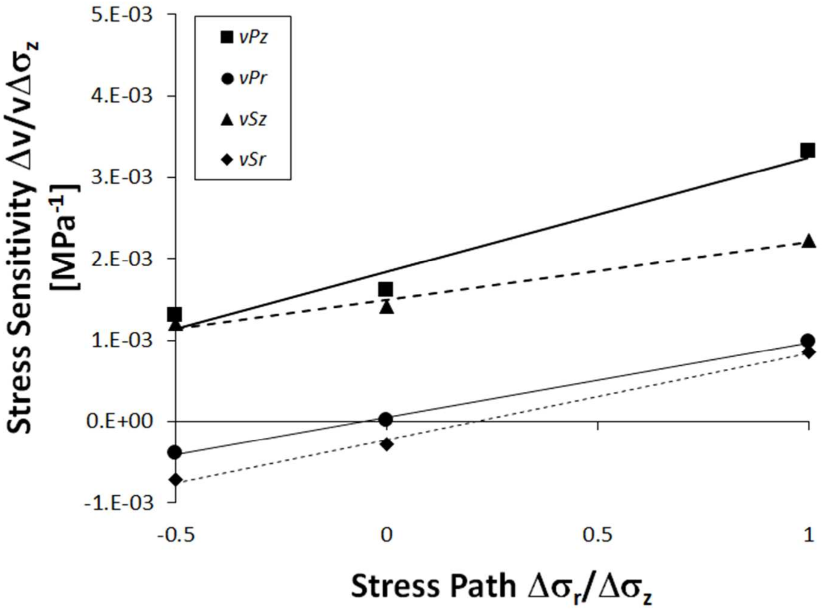
5.E-03
4.E-03
3.E-03
2.E-03
1.E-03
0.E+00
-1.E-03
-0.5
0
0.5
1
vPz
vPr
vSz
vSr
Stress Sensitivity Δv/vΔσ_z [MPa^-1]
Stress Path Δσ_r/Δσ_z

Figure 15

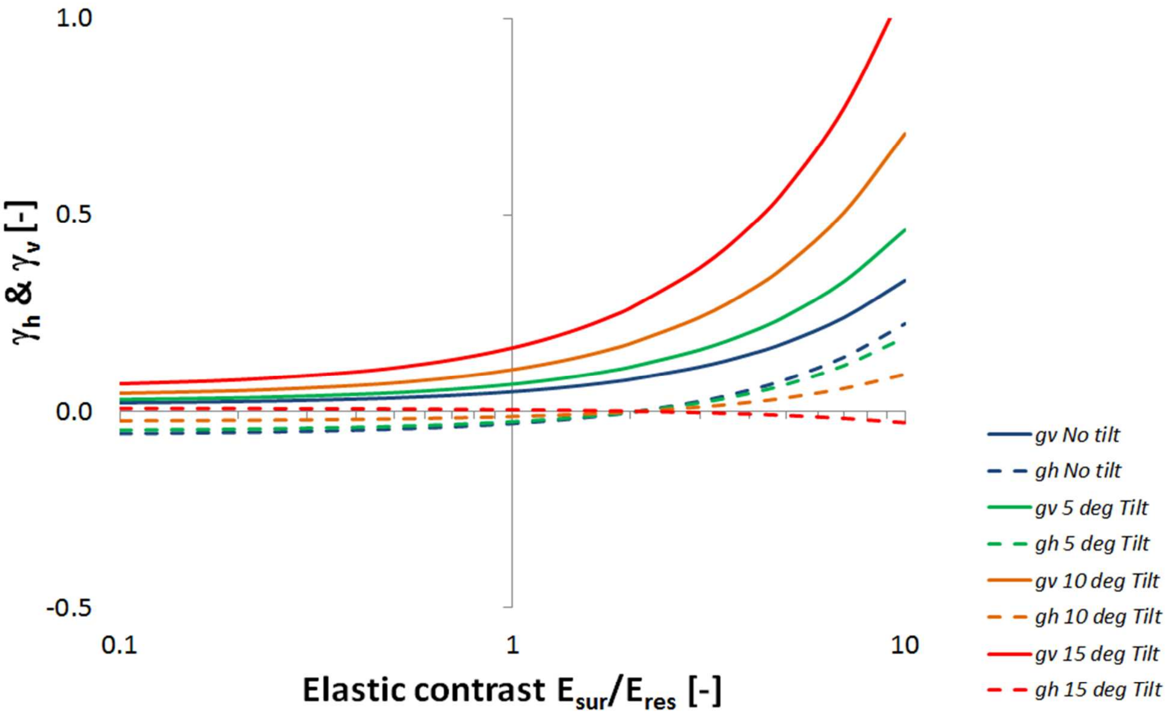
1.0
0.5
0.0
-0.5
γ_h & γ_v [-]
0.1
1
10
Elastic contrast E_{sur}/E_{res} [-]
gv No tilt
gh No tilt
gv 5 deg Tilt
gh 5 deg Tilt
gv 10 deg Tilt
gh 10 deg Tilt
gv 15 deg Tilt
gh 15 deg Tilt

Figure 16

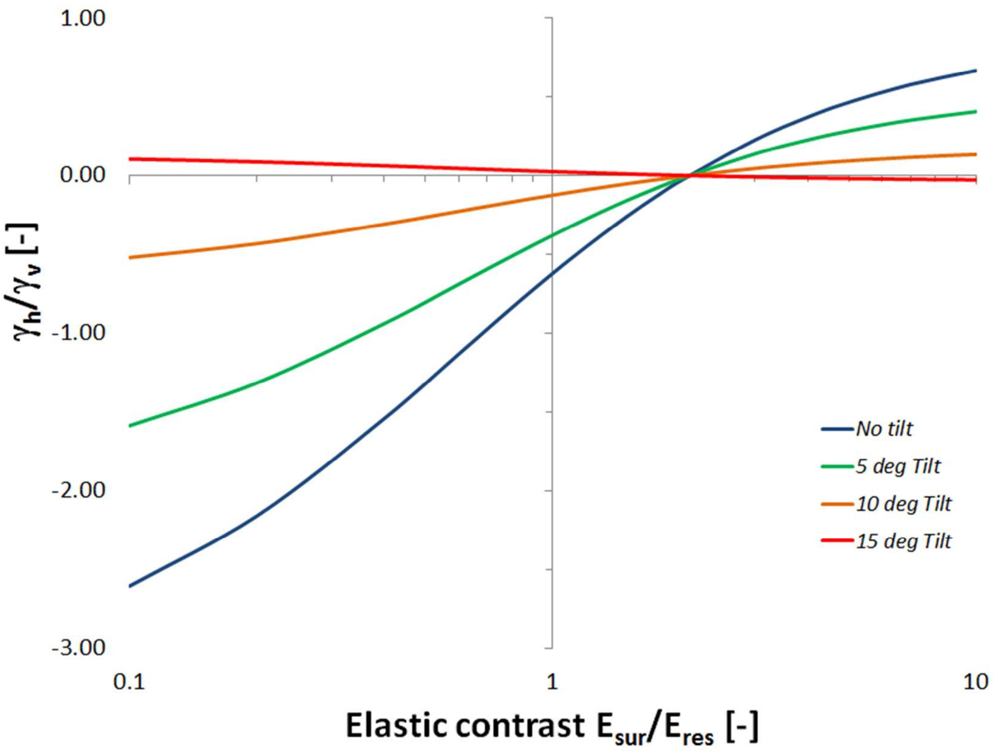
1.00
0.00
-1.00
-2.00
-3.00
γ_h/γ_v [-]
0.1
1
10
Elastic contrast E_{sur}/E_{res} [-]
No tilt
5 deg Tilt
10 deg Tilt
15 deg Tilt

Figure 17

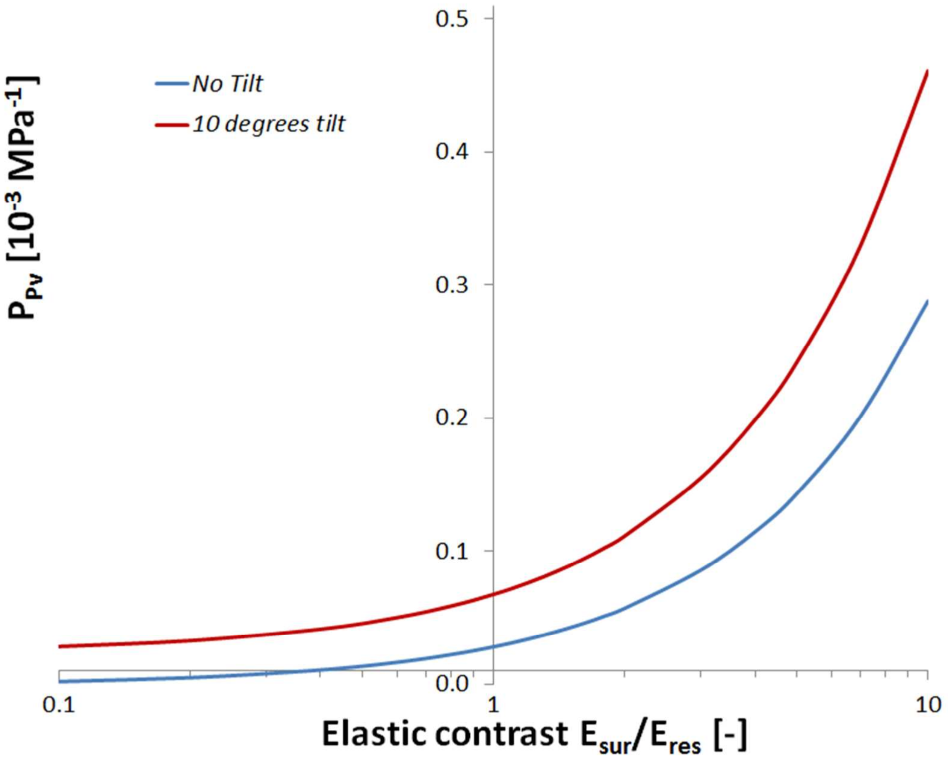
No Tilt
10 degrees tilt
P_{Pv} [10^{-3} MPa^{-1}]
0.5
0.4
0.3
0.2
0.1
0.0
0.1
1
10
Elastic contrast E_{sur}/E_{res} [-]

Figure 18

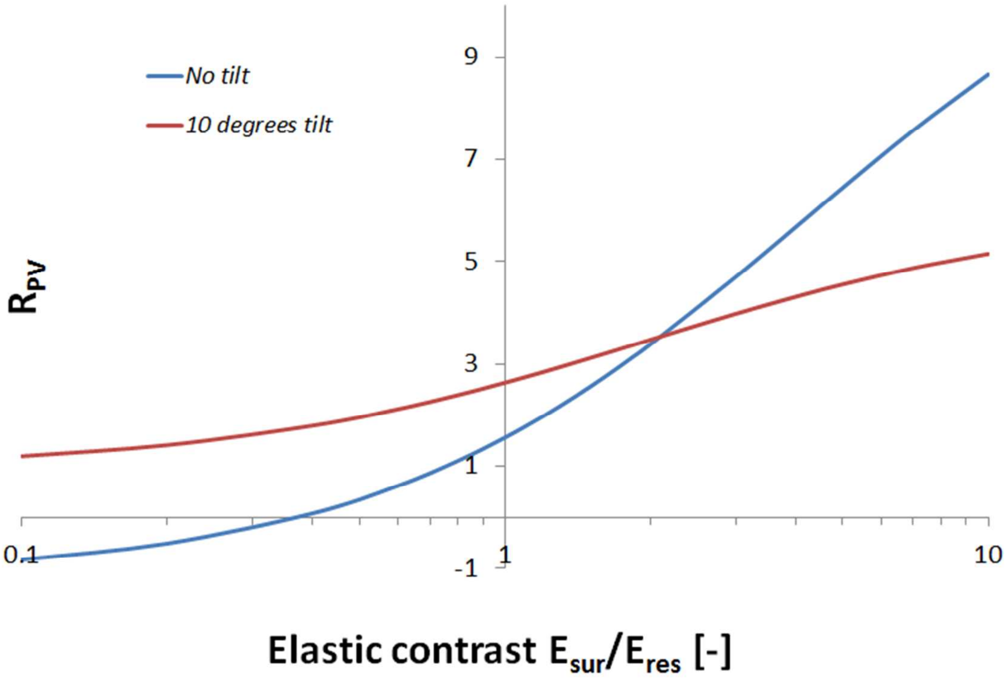
No tilt
10 degrees tilt
R$_{PV}$
9
7
5
3
1
-1
0.1
1
10
Elastic contrast E$_{sur}$/E$_{res}$ [-]

Figure 19

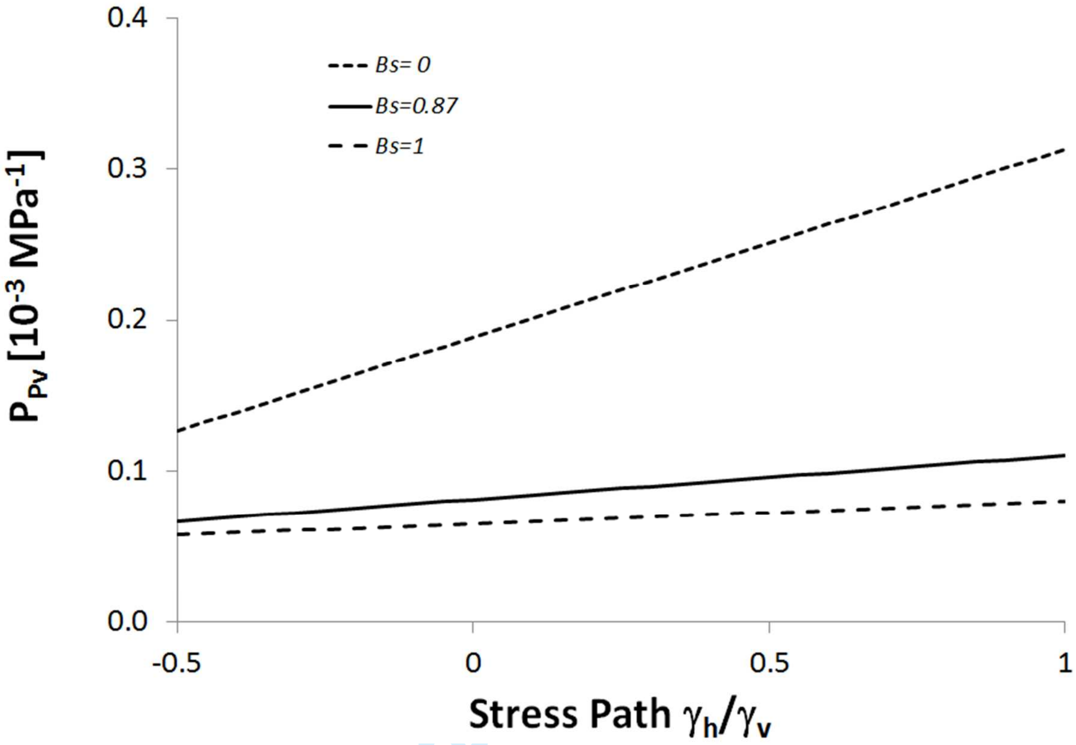
0.4
0.3
0.2
0.1
0.0
-0.5
0
0.5
1
Bs= 0
Bs=0.87
Bs=1
P_{Pv} [10^{-3} MPa^{-1}]
Stress Path γ_h/γ_v

Figure 20

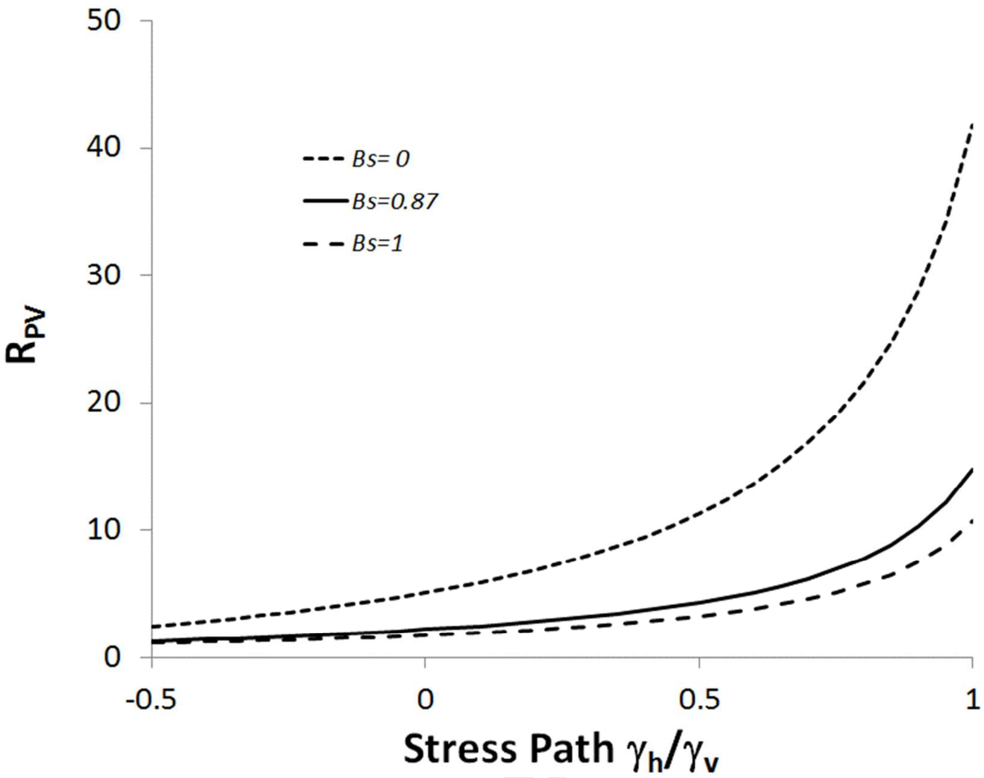
50
40
30
20
10
0
R_{PV}
Bs= 0
Bs=0.87
Bs=1
-0.5
0
0.5
1
Stress Path γ_h/γ_v

Figure 21

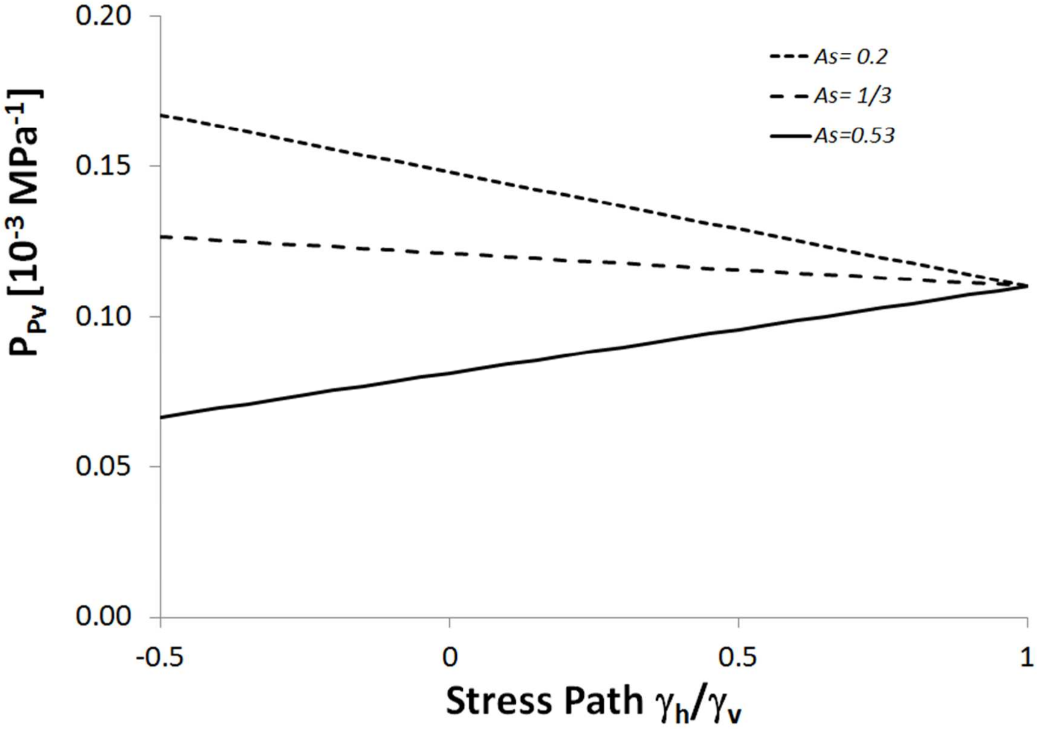
0.20
0.15
0.10
0.05
0.00
-0.5
0
0.5
1
P_{Pv} [10^{-3} MPa^{-1}]
Stress Path γ_h/γ_v
As= 0.2
As= 1/3
As=0.53

Figure 22

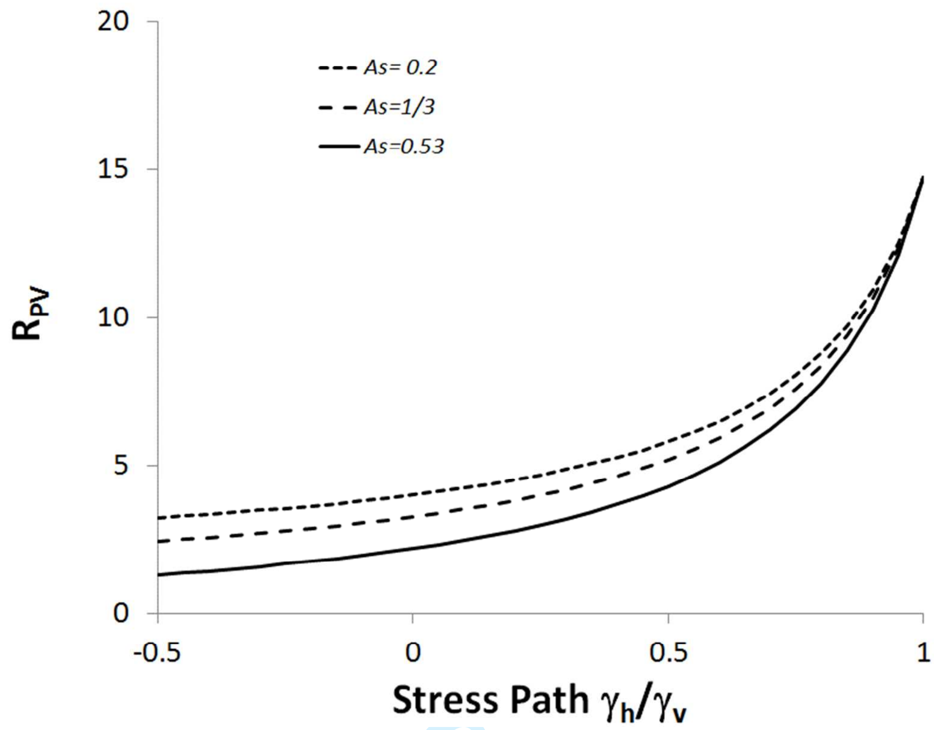
20
15
10
5
0
R_{PV}
-0.5
0
0.5
1
Stress Path γ_h/γ_v
As= 0.2
As=1/3
As=0.53

Figure 23

TABLE CAPTIONS

Table 1 Axial stress (σ_z), radial stress (σ_r) and pore pressure (p_f) representing in situ conditions in the laboratory experiments with T, D, B and M Shales. Porosity is estimated from water content, and clay content is weight percentage based on bulk XRD data. All test data presented here are obtained at room temperature.

Table 2 Ultrasonic velocities of axially and radially propagating P- and S-waves for the three brine-saturated shales (B, D and M) and for the non-saturated (T) shale.The z-axis is aligned with the symmetry axis (normal to bedding). No reliable measurement of the radial S-wave velocity (v_{Sr}) was obtained for the M shale core plug.

Table 3 Skempton A_S and B_S (Eq. (5) derived from the linear fits to the pore pressure data shown in Figure 10

Table 4 Stress sensitivity coefficients fitted to the velocity data in Figure 8 and Figure 9, using the Skempton parameters in table 3 in Eq. (7). The effective stress coefficient for isotropic stress changes n = C/A (Eq. (9)).

Table 1

Shale	σ_z [MPa]	σ_r [MPa]	p_f [MPa]	ϕ [%]	Clay content [%]
B	49.8	47.4	34.9	24	76
D	50.3	49.2	37.9	29	55
M	27.3	25.9	17.2	36	65
T	23.5	13.0	0	9	25

Table 2

Shale	v_{Pz} [m/s]	v_{Pr} [m/s]	v_{Sz} [m/s]	v_{Sr} [m/s]
B	2601	3042	1171	1528
D	2384	2652	948	1113
M	2216	2554	890	n.a.
T	3400	3806	2258	2504

Table 3

Shale	A_S	B_S
B	0.54	0.82
D	0.40	0.85
M	0.53	0.87

Table 4

Shale	A_{Pz} [10^{-3} MPa^{-1}]	B_{Pz} [10^{-3} MPa^{-1}]	C_{Pz} [10^{-3} MPa^{-1}]	n_{Pz} [-]
B	2.5	0.7	1.8	0.74
D	3.0	0.4	2.5	0.81
M	3.1	0.8	2.3	0.75
T	3.2	0.8	-	-